

JGR Space Physics

RESEARCH ARTICLE

10.1029/2018JA026291

Key Points:

- We show three cases of proton and relativistic electron precipitation observed simultaneously with EMIC waves
- EMIC-driven precipitation was observed by POES/MetOp satellites at different locations over a broad L-MLT region
- Each precipitation event extended over $\Delta L \sim 0.3$ on average, showing that wave-driven pitch angle scattering is localized

Correspondence to:

L. Capannolo and W. Li,
luisacap@bu.edu;
wenli77@bu.edu

Citation:

Capannolo, L., Li, W., Ma, Q., Shen, X.-C., Zhang, X.-J., Redmon, R. J., et al. (2019). Energetic electron precipitation: Multievent analysis of its spatial extent during EMIC wave activity. *Journal of Geophysical Research: Space Physics*, 124, 2466–2483. <https://doi.org/10.1029/2018JA026291>













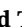

Received 12 NOV 2018

Accepted 28 FEB 2019

Accepted article online 9 MAR 2019

Published online 4 APR 2019

Energetic Electron Precipitation: Multievent Analysis of Its Spatial Extent During EMIC Wave Activity

L. Capannolo¹ , W. Li¹ , Q. Ma^{1,2} , X.-C. Shen¹ , X.-J. Zhang^{2,3} , R. J. Redmon⁴ , J. V. Rodriguez^{4,5} , M. J. Engebretson⁶ , C. A. Kletzing⁷ , W. S. Kurth⁷ , G. B. Hospodarsky⁷ , H. E. Spence⁸ , G. D. Reeves⁹ , and T. Raita¹⁰ 

¹Center for Space Physics, Boston University, Boston, MA, USA, ²Department of Atmospheric and Oceanic Sciences, University of California, Los Angeles, CA, USA, ³Department of Earth, Planetary, and Space Sciences, University of California, Los Angeles, CA, USA, ⁴Cooperative Institute for Research in Environmental Sciences, University of Colorado Boulder, Boulder, CO, USA, ⁵National Centers for Environmental Information, NOAA, Boulder, CO, USA, ⁶Department of Physics, Augsburg University, Minneapolis, MN, USA, ⁷Department of Physics and Astronomy, University of Iowa, Iowa City, IA, USA, ⁸Institute for the Study of Earth, Oceans, and Space, University of New Hampshire, Durham, NH, USA, ⁹Space Science and Applications Group, Los Alamos National Laboratory, Los Alamos, NM, USA, ¹⁰Sodankylä Geophysical Observatory, University of Oulu, Sodankylä, Finland

Abstract Electromagnetic ion cyclotron (EMIC) waves can drive precipitation of tens of keV protons and relativistic electrons, and are a potential candidate for causing radiation belt flux dropouts. In this study, we quantitatively analyze three cases of EMIC-driven precipitation, which occurred near the dusk sector observed by multiple Low-Earth-Orbiting (LEO) Polar Operational Environmental Satellites/Meteorological Operational satellite programme (POES/MetOp) satellites. During EMIC wave activity, the proton precipitation occurred from few tens of keV up to hundreds of keV, while the electron precipitation was mainly at relativistic energies. We compare observations of electron precipitation with calculations using quasi-linear theory. For all cases, we consider the effects of other magnetospheric waves observed simultaneously with EMIC waves, namely, plasmaspheric hiss and magnetosonic waves, and find that the electron precipitation at MeV energies was predominantly caused by EMIC-driven pitch angle scattering. Interestingly, each precipitation event observed by a LEO satellite extended over a limited L shell region ($\Delta L \sim 0.3$ on average), suggesting that the pitch angle scattering caused by EMIC waves occurs only when favorable conditions are met, likely in a localized region. Furthermore, we take advantage of the LEO constellation to explore the occurrence of precipitation at different L shells and magnetic local time sectors, simultaneously with EMIC wave observations near the equator (detected by Van Allen Probes) or at the ground (measured by magnetometers). Our analysis shows that although EMIC waves drove precipitation only in a narrow ΔL , electron precipitation was triggered at various locations as identified by POES/MetOp over a rather broad region (up to ~ 4.4 hr MLT and ~ 1.4 L shells) with similar patterns between satellites.

1. Introduction

The radiation belt environment is highly variable, controlled by various competing mechanisms of transport, acceleration, and loss (e.g., Reeves et al., 2003). The high-energy electron population that resides in the outer radiation belt undergoes a significant flux variability over timescales of approximately hours, mainly due to interactions between electrons and magnetospheric plasma waves. While whistler mode chorus waves play an important role in local acceleration of electrons (e.g., Horne & Thorne, 1998; Summers et al., 2002; Thorne et al., 2013; W. Li et al., 2014), magnetopause shadowing with subsequent outward radial diffusion (Hudson et al., 2014; Turner et al., 2012) and wave-driven precipitation into the upper atmosphere are the main causes of energetic electron loss (e.g., W. Li et al., 2007; Millan & Thorne, 2007; Thorne, 2010). Plasmaspheric hiss, whistler mode chorus waves, and electromagnetic ion cyclotron (EMIC) waves all contribute to the energetic electron flux dropouts in the radiation belts, but their timescales can be very different (Kersten et al., 2014; Ni et al., 2013; Summers et al., 2007; Usanova et al., 2014). On the contrary, magnetosonic waves are overall inefficient in electron losses, but have some effects in accelerating electrons (Horne et al., 2007; Ma et al., 2016). In several instances, radiation belt electron flux dropouts at relativistic

energies were observed simultaneously with EMIC wave activity (Shprits et al., 2017; Su et al., 2016; Zhang et al., 2016).

Relativistic electron precipitation (REP) causes chemical changes in the Earth's upper stratosphere and lower thermosphere by enhancing production of nitrogen oxides ($\text{NO}_x = \text{N}, \text{NO}, \text{NO}_2$) and hydrogen oxides ($\text{HO}_x = \text{H}, \text{OH}, \text{HO}_2$; Mironova et al., 2015; Sinnhuber et al., 2012). These compounds are known to induce ozone reduction (Meraner & Schmidt, 2018), thus potentially impact atmospheric circulation and eventually climate. Identifying the drivers of high-energy electron precipitation is therefore important to shed light not only on radiation belt loss mechanisms but also on atmospheric dynamics.

In the magnetosphere, EMIC waves have a frequency range of 0.1–5 Hz and typically occur in three distinct bands separated by the hydrogen (f_{CH}), helium (f_{CHe}), and oxygen (f_{CO}) cyclotron frequencies (Erlandson & Ukhorskiy, 2001; Fraser et al., 2010). They mainly propagate along magnetic field lines and are detectable by ground-based magnetometers as Pc1 and Pc2 waves (Engebretson et al., 2008) over a wider latitudinal range due to ionospheric ducting (Kim et al., 2010). EMIC waves are generated in the magnetosphere by anisotropic distributions of energetic ions and tend to occur frequently during geomagnetic activity, when ring current ions are injected from the magnetotail into the inner magnetosphere (Fraser et al., 2010; Jordanova et al., 2008). H-band EMIC waves dominate near the dawn sector, whereas He-band activity occurs more frequently near the dusk sector (Allen et al., 2016; Min et al., 2012). Coordinated measurements from the available spacecraft and ground observations allowed Engebretson et al. (2015) to identify the significantly wide spatial extent of the EMIC wave activity on 23 February 2014, which covered over 8 hr in UT and 12 hr in magnetic local time (MLT). Similarly, using multipoint observations from Van Allen Probes, Blum et al. (2017) statistically showed that dayside EMIC waves are more spatially extended, while nightside EMIC waves span a narrower MLT and persist longer.

Since both protons and electrons can interact with EMIC waves via cyclotron resonance, typical signatures of EMIC-driven precipitation show simultaneous precipitation of tens of keV protons and relativistic electrons (Carson et al., 2012). Statistical studies reveal that such events occur mainly in the afternoon-midnight sector (Shekhar et al., 2018; Yahnin et al., 2017), in agreement with the favorable location of EMIC wave enhancements in association with ring current injections (Morley et al., 2009; Pickett et al., 2010; Usanova et al., 2008). A recent study by Hirai et al. (2018) showed direct evidence of correlation between the rising tone EMIC wave structure and the associated bursts of REP. Pitch angle scattering of ring current protons (~ 10 s of keV) driven by EMIC waves has been often associated with proton aurora (Cao et al., 2016; Miyoshi et al., 2008; Summers et al., 2017; Xiao et al., 2011; Yuan et al., 2010).

While it is known that EMIC waves can drive precipitation of energetic electrons, the minimum energy (E_{min}) of electrons that are subject to efficient pitch angle scattering is still under active investigation (Capannolo et al., 2018; Hendry et al., 2017; Miyoshi et al., 2008). Considering resonant wave/particle interactions and cold plasma theory, E_{min} could be as low as several hundred keV, depending on various parameters, such as wave frequency spectrum, plasma density, and ion composition (Summers & Thorne, 2003; W. Li et al., 2007; Meredith et al., 2014; Ni et al., 2015). However, warm plasma effects can modify the cold plasma dispersion relation, which ultimately limits the actual value of E_{min} to >1 MeV (Chen et al., 2011; Silin et al., 2011). Moreover, theoretical studies by Chen et al. (2016) suggest that EMIC waves can scatter electrons via nonresonant interactions, lowering the E_{min} to a few hundred keV. Such a result might explain the lower E_{min} peaking at ~ 300 keV reported by Hendry et al. (2017).

The presence of EMIC waves, however, does not necessarily drive electron precipitation under all conditions. For example, statistical studies by Yahnin et al. (2016, 2017) show that only few REP events occur in association with EMIC wave activity detected on the ground. Similarly, Qin et al. (2018) found that, among 473 conjunction events in association with EMIC waves, only 127 show REP events, of which 30% occur when H-band and He-band EMIC waves coexist. The EMIC activity on 11 October 2012, studied by Usanova et al. (2014), did not coincide with REP, most likely because of the absence of electron flux at intermediate to low pitch angles, where EMIC wave scattering is more efficient.

Although previous studies have provided evidence of EMIC-driven precipitation, its spatiotemporal extent is not clear and still needs further analysis. A case study by Z. Li et al. (2014) reports a precipitation event in association with EMIC waves observed at different times by three balloons belonging to the Balloon Array

for Radiation-belt Relativistic Electron Losses (BARREL) mission (Millan et al., 2013). For BARREL 1G, the precipitation lasted ~ 20 min and occurred at MLT ~ 22 and $L \sim 6.5$; however, no further investigation was conducted on the REP events observed by the other two balloons. Blum et al. (2015) also used BARREL to relate EMIC waves to the observed precipitation over 18–19 January 2013, but the precipitation events were almost 1 day apart and most likely not related to the same EMIC waves. The REP event around the end of 18 January 2013 was further analyzed by Clilverd et al. (2017): precipitation was observed by BARREL 1C and BARREL 1D, at different times and locations. They concluded that these observations could be explained as duskside precipitation patches drifting westward with sizes of 1.5–3.5 hr in MLT.

In this study, we take advantage of the highly inclined Low-Earth-Orbiting (LEO) satellite constellation to study the electron precipitation in the upper atmosphere resulting from interactions with magnetospheric waves simultaneously observed in the radiation belts. We also analyze the L shell extent and duration of the observed precipitation in the upper atmosphere. A similar approach was used in the statistical study by Shekhar et al. (2017); however, we focus our analysis only on precipitation events occurring during EMIC wave activity observed in the magnetosphere or at ground stations and also consider the precipitation pattern observed at the full energy range of electrons and protons provided by Polar Operational Environmental Satellites (POES)/Meteorological Operational satellite programme (MetOp). Finally, using quasi-linear theory we quantify the efficiency of observed plasma waves in causing electron precipitation through pitch angle scattering and compare the results to observations. We show three case studies, all occurring near the duskside. We describe the data and methodology in section 2. Section 3 presents the case studies, followed by the comparison between observations and quasi-linear theory predictions in Section 4. We summarize and discuss the results in section 5.

2. Satellite Data and Methodology

The twin Van Allen Probes (or Radiation Belt Storm Probes, RBSP) orbit near the magnetic equator with a 9-hr period and $\sim 10^\circ$ inclination and provide in situ equatorial measurements of magnetospheric waves for this study. RBSP-A and RBSP-B have a perigee of ~ 600 km and an apogee of $\sim 6 R_E$ (Mauk et al., 2013). The Electric and Magnetic Field Instrument Suite and Integrated Science (EMFISIS) Waves instrument provides a comprehensive set of magnetospheric wave properties through measuring magnetic and electric fields with frequencies from ~ 10 Hz up to 400 kHz (Kletzing et al., 2013). The triaxial fluxgate magnetometer provides the magnetic field vector and low-frequency waves (< 32 Hz). Plasma density is inferred from the upper hybrid resonance frequency detected by the High-Frequency Receiver (Kurth et al., 2015). Van Allen Probes also provide particle measurements, such as pitch angle and energy distributions of protons and electrons, as detected by the Energetic Particle, Composition, and Thermal Plasma Suite (ECT; Spence et al., 2013).

Low-altitude observations are provided by the National Oceanic and Atmospheric Administration (NOAA) POES and the European Organisation for the Exploitation of Meteorological Satellites (EUMETSAT) MetOp constellation (Evans & Greer, 2004). Each satellite orbits at an altitude between 800 and 850 km with an orbital period of ~ 100 min. The spacecraft are Sun-synchronous and operate in different local time planes. The Medium Energy Proton and Electron Detector measures electron and proton count rates with a telescope oriented to zenith (0° telescope) and one perpendicular to it (90° telescope), allowing us to distinguish between the precipitating and the trapped or quasi-trapped populations. In this study, we use the proton channels P1 (30–80 keV), P2 (80–250 keV), and P3 (250–800 keV) and the electron channels E2 (> 130 keV) and E3 (> 287 keV). The proton channel P6 (> 6.9 MeV) is mainly contaminated by electrons > 700 –800 keV and thus can be used as a virtual electron channel (E4) when no signal is detected by the proton channel at lower energy (P5, 2.5–6.9 MeV), which is not sensitive to electrons (Carson et al., 2012; Green, 2013; Rodger et al., 2010; Yando et al., 2011). The E4 channel is thus used as a relativistic electron detector, given its effective energy at ~ 879 keV (Peck et al., 2015). It is worthwhile to note that the electron channels can be contaminated by protons of energies ~ 210 –2700 keV (Rodger et al., 2010; Yando et al., 2011), which we remove using the method described in Peck et al. (2015). We use the 2-s time resolution for POES data and show fluxes converted from count rates using the geometric factors in Table 3–2 in Green (2013). While unphysical, the proton trapped flux is sometimes lower than the precipitating value (Lyons & Evans, 1984). This effect arises because proton channels (especially those for the 90° telescope) are affected by radiation damage over time, and such detector degradation determines a higher energy threshold than

the nominal one (e.g., Asikainen et al., 2012; Dubyagin et al., 2018; Galand & Evans, 2000; Sandanger et al., 2015).

For this study, we consider precipitation events occurring during EMIC wave activity when RBSP and POES/MetOp are roughly along the same magnetic field line ($\Delta\text{MLT} \leq 0.5$ and $\Delta L \leq 0.5$). In order to study the spatial extent of the observed precipitation, once we identify a close magnetic conjunction event, we search for similar precipitation patterns occurring during the same EMIC wave event but detected by other POES or MetOp nearby. To support EMIC wave observations when RBSP is not in conjunction with POES satellites, we use the available ground-based magnetometer stations to search for potential EMIC wave activity.

Analyzing events that occur during magnetic conjunctions is essential to understand the relation between the precipitation observed at low altitudes and the wave drivers in the magnetosphere or at the ground. For the identified tightest magnetic conjunctions, we use quasi-linear theory (Ni et al., 2015; Summers, 2005) to quantify the efficiency of the observed magnetospheric waves in pitch angle scattering, which is then compared to the low altitude electron observations.

3. Observations

Despite magnetic conjunctions between RBSP and POES/MetOp occur frequently, interesting case studies for EMIC-driven precipitation are quite rare for the following two reasons: (1) conjunctions need to occur during EMIC wave activity and (2) EMIC waves must be strong enough to drive electron precipitation so that POES/MetOp satellites detect a clear electron flux signal above the noise level. Out of all the numerous conjunctions identified during EMIC wave activities observed from 2012 to 2017, we selected three cases for in-depth analysis since these showed at least one very tight magnetic conjunction between EMIC wave observations (RBSP or ground-based magnetometers) and interesting patterns of precipitation detected by the POES/MetOp satellite constellation at various ranges of MLT sectors and L shells. These three cases occurred over 20:05–20:21 UT on 10 September 2015 (Case study 1), over 20:14–20:54 UT on 28 February 2015 (Case study 2), and over 11:32–13:21 UT on 24 September 2013 (Case study 3). Electron precipitation was observed near the duskside, mostly inside the plasmapause, where we expect more efficient pitch angle scattering driven by EMIC waves. The case studies also occurred in absence of other strong magnetospheric waves, which can be effective in causing energetic electron precipitation as well, thus allowing us to identify the main driver of pitch angle scattering without ambiguity.

3.1. Case Study 1: 10 September 2015

Wave observations by RBSP-A are shown in Figure 1, followed by the POES precipitation and the L-MLT polar plot of the precipitation events in Figure 2. This event occurred during the recovery phase of a substorm with AL reaching almost -800 nT (Figure 1a). RBSP-A observed EMIC wave activity from 19:35 UT up until 20:21 UT (marked by a red horizontal bar on the X axis in Figure 1), spanning MLT of 17.9–19.1 and L shells of 3.6–4.9, during an inbound orbit within the plasmasphere (density $100\text{--}300\text{ cm}^{-3}$; Figure 1b). The EMIC waves were in the He-band frequencies at high L and until ~ 20 UT and became dominant in the H-band at lower L shells (Figure 1g). Simultaneously with this EMIC wave activity, hiss and magnetosonic waves were also observed by RBSP-A (Figures 1c and 1d), with wave ellipticity and normal angle shown in Figures 1e and 1f, respectively. The white dashed lines indicate the UT time of precipitation at low orbit observed by POES, the magenta dashed-dot line indicates the UT time of the tightest POES/RBSP-A conjunction (with NOAA-15 at $L = 4.1$) and the solid magenta lines show the L range of ± 0.5 around it.

Figures 2A and 2B show the proton and electron fluxes as measured respectively by NOAA-15 and NOAA-18 during the EMIC wave activity. The trapped (precipitating) flux measured by the 90° (0°) POES telescope is shown with the double-dot-dashed line (solid line). Different colors indicate the different energy channels for protons (P1 30–80 keV in black, P2 80–250 keV in blue, and P3 250–800 keV in red) and electrons (E2 > 130 keV in black, E3 > 287 keV in green, and E4 > 612 keV in red). It is worthwhile to note that >40 keV electron channel (E1) is not shown, since it is potentially subject to significant proton contamination. The tightest L-MLT conjunction with RBSP-A occurred for NOAA-15 (Figure 2A), for which we calculated the ratios of precipitating (E_0) to trapped (E_{90}) electron flux ($R = E_0/E_{90}$) color coded by energy during the precipitation interval highlighted by the gray shaded region. Figures 2A and 2B show the simultaneous precipitation of protons and electrons at $\sim 20:05:00$ UT for NOAA-15 and at $\sim 20:20:30$ UT for NOAA-18,

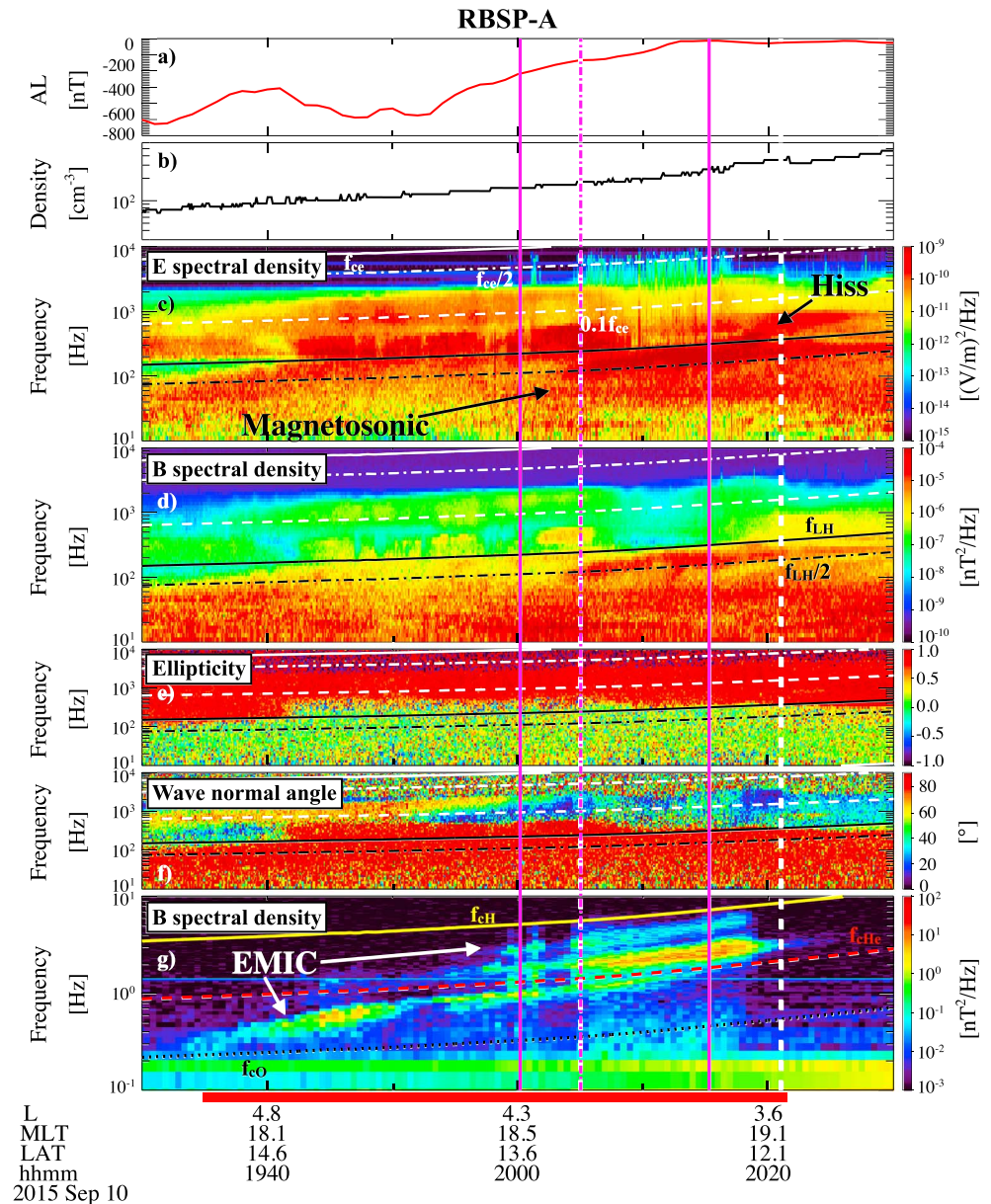


Figure 1. Observations from RBSP-A on 10 September 2015. (a) AL index, (b) density, (c) electric and (d) magnetic field spectral density from EMFISIS, (e) ellipticity, (f) wave normal angle, and (g) magnetic field spectral density showing EMIC waves. The frequency lines in the spectrograms are electron cyclotron frequency f_{ce} (white solid), $0.5 f_{ce}$ (white dashed dot), $0.1 f_{ce}$ (white dashed), lower hybrid resonance frequency f_{LH} (solid black), $0.5 f_{LH}$ (black dashed dot), proton cyclotron frequency f_{cH} (yellow solid), helium cyclotron frequency f_{cHe} (red dashed), and oxygen cyclotron frequency f_{cO} (black dotted). The vertical white dashed lines correspond to the beginning and end of the precipitation time interval observed by POES; the magenta dash-dot line indicates the UT time of precipitation with NOAA-15 (tightest conjunction) and the magenta solid lines show the ± 0.5 L interval around the precipitation L shell. The red bar at the bottom shows the UT time of EMIC wave activity detected along the RBSP-A trajectory (a thick red line) in Figure 2C. EMIC = electromagnetic ion cyclotron; RBSP = Radiation Belt Storm Probes; MLT = magnetic local time.

suggesting that the precipitation driven by magnetospheric waves occurred at least within a 15-min window. The proton precipitation was strongest in the P1 channel for both spacecraft but was also significant in P2 and P3 for NOAA-15. The electron precipitation occurred mainly in the E4 channel at both satellites, since the precipitating fluxes at >130 keV ($E2_0$, solid black line) and >287 keV ($E3_0$, solid green line) were approximately the same as the >612 keV precipitating electrons ($E4_0$, solid red line). On top of the

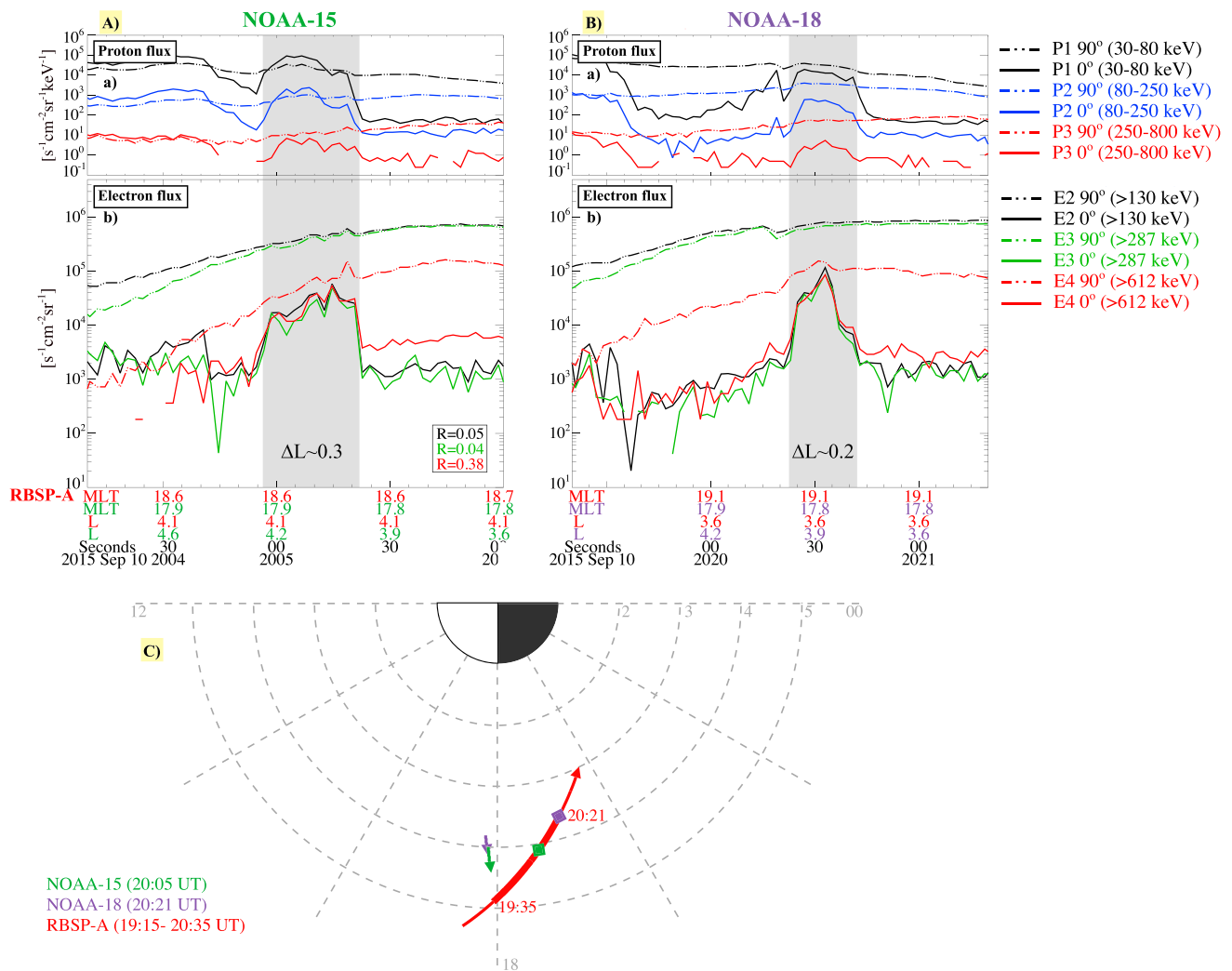


Figure 2. An overview of particle precipitation observed on 10 September 2015 from NOAA-15 (A) and NOAA-18 (B). The X axis shows the MLT and L shell color coded for RBSP-A (red), NOAA-15 (green), and NOAA-18 (purple). (a) Proton flux in the P1 (30–80 keV) channel (black), P2 (80–250 keV, blue), and P3 (250–800 keV, red). (b) Electron flux in the E2 channel (>130 keV, black), E3 (>287 keV, green), and E4 (>612 keV, red) as a function of UT, L shell, and MLT. Double-dot-dashed lines are for trapped fluxes, and solid lines are for precipitating fluxes. The gray areas represent the UT interval of electron precipitation. In column (A), R indicates the precipitating-to-trapped ratio calculated and color coded in each electron energy. (C) L-MLT polar plot with noon to the left: NOAA-15 and NOAA-18 trajectories during the observed precipitation (gray areas in A and B) are depicted with the green and purple arrows, respectively; the time stamps in the legend indicate the precipitation UT time for NOAA-15 (green) and NOAA-18 (purple); RBSP-A trajectory between 19:15 and 20:35 UT is in red, where thicker lines indicate EMIC wave observations with the starting and ending time marked with the red time stamps. The colored diamonds on top of RBSP-A trajectory indicate the RBSP-A location at the UT time of precipitation observed by NOAA-15 (green diamond) and NOAA-18 (purple diamond). NOAA = National Oceanic and Atmospheric Administration; RBSP = Radiation Belt Storm Probes; MLT = magnetic local time.

gray shaded regions, we also marked the L shell extent of each precipitation event: 0.3 (~25 s) and 0.2 L (~20 s) shells for NOAA-15 and NOAA-18, respectively.

Figure 2C summarizes the geometry of the event in a polar L-MLT plot. We show the trajectories of NOAA-15 (green) and NOAA-18 (purple) during the precipitation intervals (gray shaded areas in Figures 2A and 2B) and RBSP-A (red) over 19:15–20:35 UT. The thicker red line indicates EMIC wave observations made by RBSP-A. The diamonds on top of the RBSP-A trajectory indicate the RBSP-A location at the UT time of precipitation detected by NOAA-15 (green) and NOAA-18 (purple). For this event, the precipitation pattern is very similar for both NOAA-15 and NOAA-18, allowing us to conclude that the precipitation occurred over 3.8–4.2 in L shell and ~1 hr in MLT (considering observations from RBSP-A, NOAA-15, and NOAA-18). It is very likely that the precipitation region extends further in MLT and L; however, no other POES/MetOp

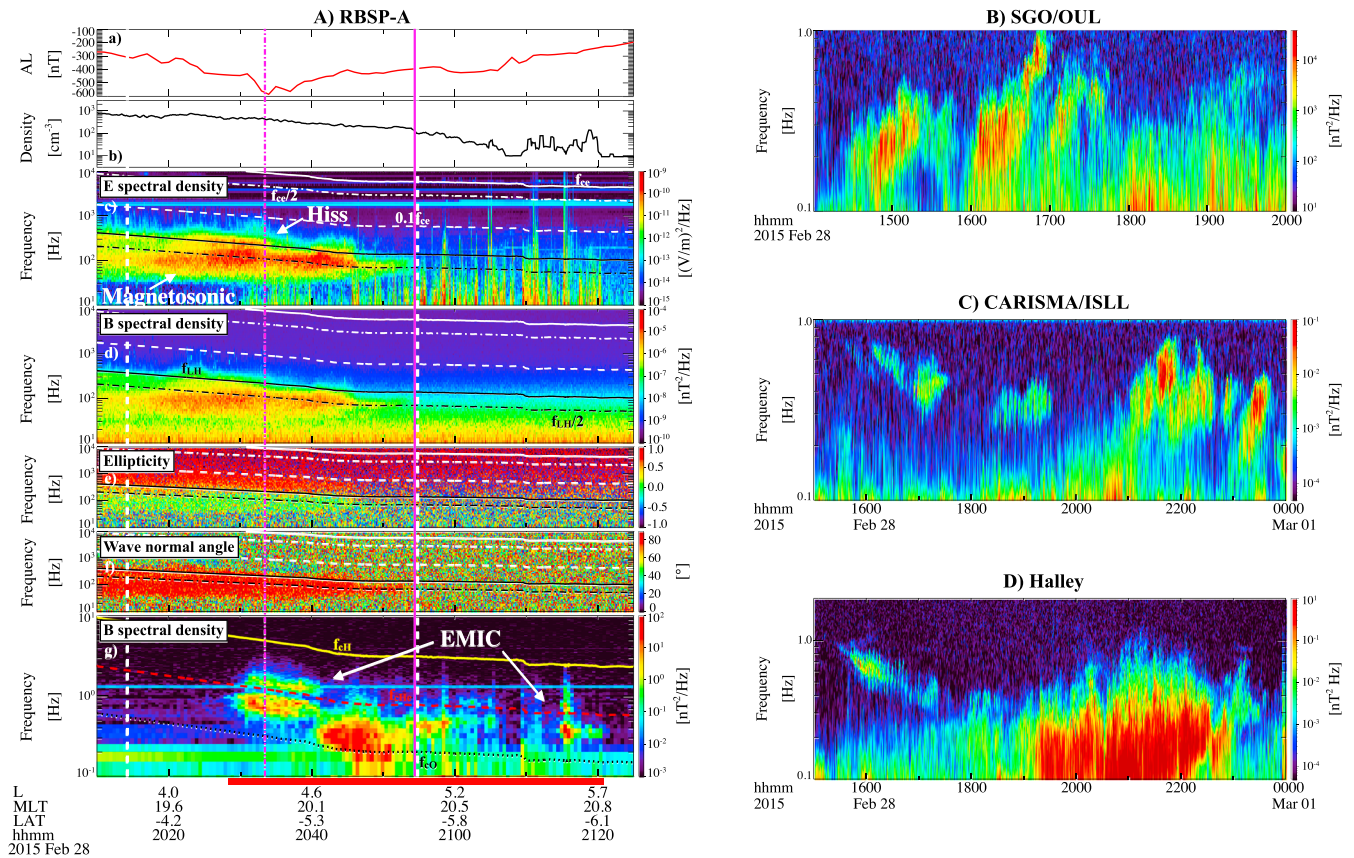


Figure 3. Observations from RBSP-A (A) and ground-based magnetometers on 28 February 2015 (B–D). Panel (a)–(g) have the same format as Figures 1a–1g. The vertical white dashed lines correspond to the beginning and end of precipitation UT time interval observed at POES; the magenta dash-dot line indicates the UT time of precipitation with MetOp-01 (tightest conjunction) and the magenta solid line show the $+0.5$ L interval around the precipitation L shell (the other extreme at -0.5 L shell is to the left, outside the UT time plotted). The red bar at the bottom shows the UT time of EMIC wave activity detected with a thick red line along the RBSP-A trajectory in Figure 4E. Panels (B)–(D) show the ground-based observations of the EMIC wave spectra at SGO/OUL, CARISMA/ISLL, and Halley. We show the total magnetic field power spectral density as a function of frequency and time. EMIC = electromagnetic ion cyclotron; RBSP = Radiation Belt Storm Probes; MLT = magnetic local time; CARISMA = Canadian Array for Realtime Investigations of Magnetic Activity.

spacecraft were available in that region during the EMIC wave observations. Therefore, this analysis can only provide a lower limit of the extent of precipitation events.

3.2. Case Study 2: 28 February 2015

Figure 3 shows the wave data observed by RBSP-A and three ground-based stations, followed by the corresponding POES/MetOp observations in Figure 4. Near the end of the expansion phase and early recovery phase of a substorm, RBSP-A observed EMIC waves over 20:28–21:20 UT (Figure 3Ag), during an outbound orbit in the plasmasphere (average density ~ 100 cm⁻³, inferred from the upper hybrid frequency line). Over 20:28–20:42 UT ($L = 4.3$ – 4.6 , MLT = 19.8–20.1), both He-band and H-band waves existed, whereas at higher MLT and L shells the EMIC waves occurred mainly below f_{cHe} , with the exception of the double-band EMIC waves at $\sim 21:15$ UT (MLT ~ 20.7 , $L \sim 5.6$). This EMIC wave was triggered by ~ 10 s of keV ion injections from the magnetotail (not shown) observed by the HOPE (Helium, Oxygen, Proton, Electron) spectrometer at $\sim 20:20$ UT. Simultaneously with the EMIC activity, magnetosonic waves and weak hiss were observed as well, followed by time domain structures dominating at L shells above ~ 5 . For this case, since precipitation was observed over a wider L-MLT range than that covered by RBSP-A (see details later regarding Figure 4 description), we also show EMIC wave activity detected at the ground. More specifically, we show EMIC spectra (total power) recorded by the OUL station in the Finnish array (14–20 UT, MLT \sim UT + 2, $L = 4.6$; Figure 3B), CARISMA (Canadian Array for Realtime Investigations of Magnetic Activity) ISLL station (15–24 UT, MLT \sim UT - 6, $L = 5.15$, Figure 3C), and Halley (15–24 UT, MLT \sim UT - 3, $L = 4.7$, Figure 3D).

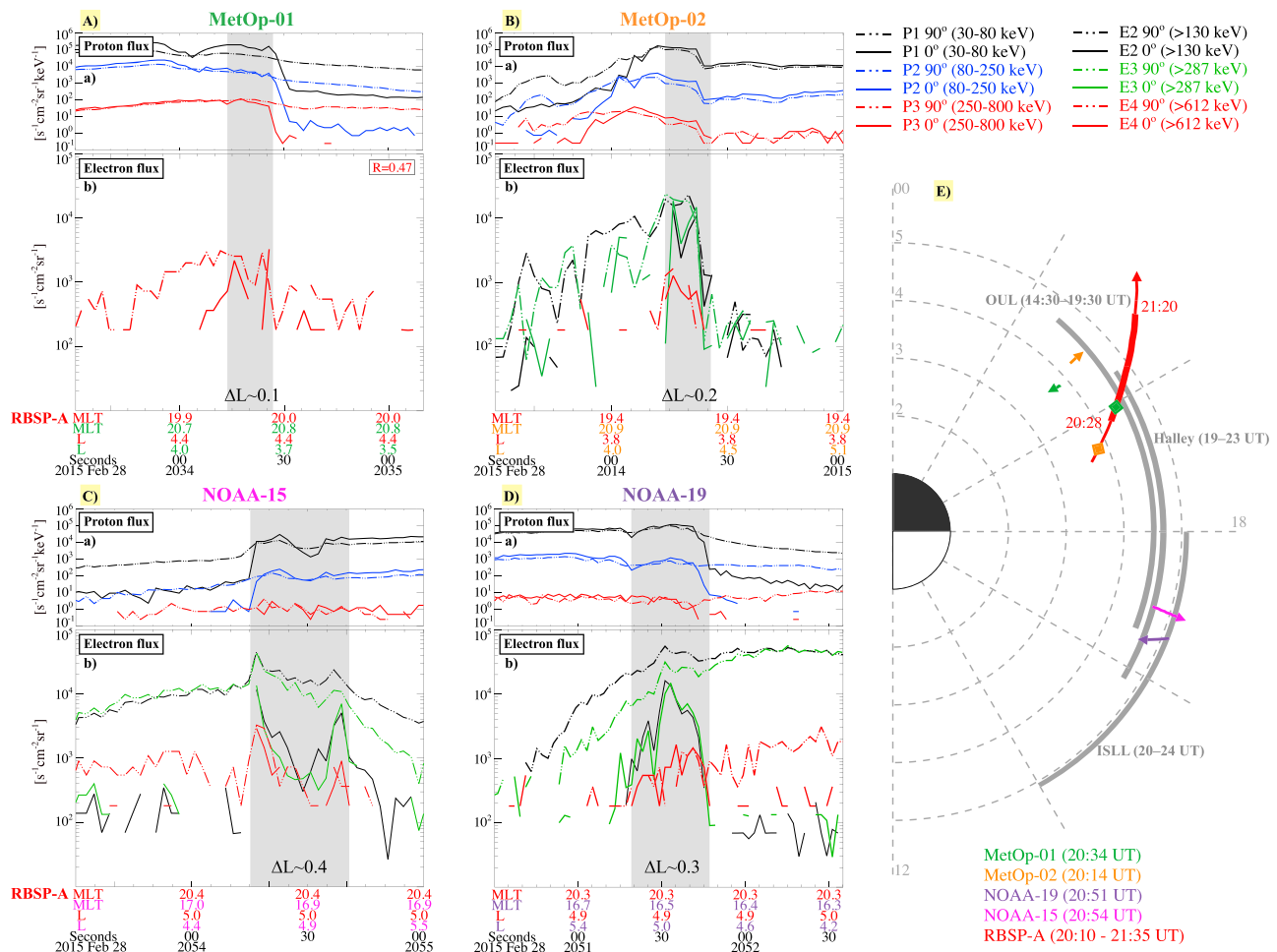


Figure 4. An overview of particle precipitation observed on 28 February 2015 from MetOp-01 (A), MetOp-02 (B), NOAA-15 (C), and NOAA-19 (D) with the similar format to Figure 2. (E) L-MLT polar plot with noon to the bottom: MetOp-01, MetOp-02, NOAA-15, and NOAA-19 trajectories during observed precipitation (gray areas in A–D) are in green, orange, magenta and purple, respectively; the time stamps in the legend indicate the precipitation UT time for MetOp-01 (green), MetOp-02 (orange), NOAA-15 (magenta), and NOAA-19 (purple); RBSP-A trajectory between 20:10 and 21:35 UT is in red, where thicker lines indicate EMIC wave observations with the starting and ending time marked with the red time stamps. The RBSP-A location at the UT time of observed precipitation for MetOp-01 and MetOp-02 is indicated with a green and an orange diamond, respectively. Gray arcs represent observations at ground-based magnetometer stations at SGO/OUL, CARISMA/ISLL and Halley mapped in the L-MLT plane, where the time interval of the detected EMIC wave activity was marked. MetOp = Meteorological Operational satellite programme; NOAA = National Oceanic and Atmospheric Administration; EMIC = electromagnetic ion cyclotron; RBSP = Radiation Belt Storm Probes; MLT = magnetic local time.

Figure 4 illustrates the precipitation events with a similar format to Figure 2. For MetOp-01 (operationally MetOp-B, Figure 4A), in closest conjunction with RBSP-A, we only show the E4 channel, since E1, E2, and E3 channels were potentially subject to severe proton contamination. Electron precipitation (highlighted by the gray shaded areas) was associated with proton precipitation. It is worth noting that clear and isolated proton precipitation can be observed only for NOAA-15 (Figure 4C) and NOAA-19 (Figure 4D), while the proton precipitation patterns for the MetOp satellites (especially for MetOp-02, operationally MetOp-A, Figure 4B) seem to resemble signatures of current sheet scattering effects, with the precipitation of higher energy protons (i.e., P3) occurring at lower L shells than lower-energy protons (i.e., P1), as also found by Yahnin et al. (2016). However, the signatures of EMIC-driven proton precipitation can still be embedded into such flux patterns, as the strong electron precipitation suggests (Yahnin et al., 2017). Current sheet scattering effects tend to be more evident near the night sector and correspond to the region where the curvature radius of the magnetic field lines is comparable to the proton gyroradius (Gilson et al., 2012). Therefore, it is reasonable that NOAA-15 and NOAA-19 (predusk sector) did not show these effects significantly.

The proton precipitation was strong across all P channels, whereas electrons seemed to have the strongest precipitation in E4. For MetOp-02, NOAA-15, and NOAA-19 there was significant E3 precipitation as well ($E_{20} \sim E_{30} > E_{40}$), suggesting that scattering into the loss cone occurred for electrons at energies potentially as low as ~ 300 keV. The L shell extent of electron precipitation was narrower ($\Delta L \sim 0.1\text{--}0.2$) in the postdusk sector but was more extended in the pre-dusk sector ($\Delta L \sim 0.3\text{--}0.4$). This suggests that the EMIC waves observed in the postdusk sector by RBSP-A may have a different spatial extent and spectral properties than those observed in the predusk sector but still cause electron precipitation.

Figure 4E shows the summary of the precipitation events in an L-MLT polar plot. We plot the trajectories of the LEO satellites only during the time interval of the observed precipitation (20:14–20:54 UT). MetOp-01 (green) and MetOp-02 (orange) were in conjunction with RBSP-A (red, shown over 20:10–21:35 UT), which detected EMIC waves from 20:28 to 21:20 UT (thicker red line). Note that during the MetOp-02 precipitation, RBSP-A did not observe EMIC wave activity; however, this effect is probably caused by spatial effects: the L and MLT values between the two satellites differ significantly. In fact, once RBSP-A approached the L shell of MetOp-02 ($L \sim 4.4$), it detected EMIC waves. NOAA-15 and NOAA-19 were far from being in conjunction with RBSP-A; however, their precipitation signature was still likely EMIC-driven, given ground observations of EMIC waves simultaneously at OUL, Halley, and ISLL (gray arcs). In summary, all four spacecraft show a similar pattern of electron precipitation occurring in a rather large L-MLT range (MLT $\sim 16.5\text{--}20.9$ and $L \sim 3.7\text{--}5.1$).

3.3. Case Study 3: 24 September 2013

Figure 5 shows wave observations from both RBSP, followed by the particle precipitation data in Figure 6. The precipitation during the MetOp-01/RBSP-A conjunction at $\sim 12:41$ UT has been studied in depth in Capannolo et al. (2018). Here we use other nearby POES satellites to study the L-MLT extent of such precipitation.

Figure 5A shows wave data from RBSP-A: EMIC waves were observed over $\sim 11:30\text{--}13:00$ UT (red horizontal band, panel g) inside the plasmasphere (Figure 5Ab), simultaneously with ~ 10 s of keV proton injections (shown in Figure 1 in Capannolo et al., 2018), dominant in the He-band, but extending partially in the H-band as well, especially at lower L shells. Simultaneously, hiss and magnetosonic waves were also observed during the inbound orbit of RBSP-A. Figure 5B shows the wave observation from the RBSP-B outbound orbit: weak He-band waves were observed at around ~ 13 UT and with stronger intensities after 13:20 UT in both H-band and He-band, highlighted by the light blue horizontal bars (panel g). It is worthwhile to note that these EMIC waves were observed in the high-density region inside the plasmasphere (Figure 5Bb). Very weak hiss and magnetosonic waves were also detected from $\sim 12:30$ to $\sim 13:50$ UT. During these observations, both probes were in the plasmasphere with densities of ~ 100 cm³. Engebretson et al. (2018) extensively showed additional EMIC wave observations occurring during this day, observed by ground-based magnetometers (i.e., CARISMA, STEL, and Halley), confirming that the wave activity persisted for hours and covered a large region in L shells and MLT (see Figure 5e in Engebretson et al., 2018).

POES observations and the L-MLT polar plot summary are shown in Figure 6, with the similar format to that of Figures 2 and 4. The in-depth analysis of the MetOp-01 observations was performed in Capannolo et al. (2018), where all electron energy channels (corrected from proton contamination following Peck et al., 2015) were shown. However, after a more careful comparison between P2-P3 and E1-E2-E3, the proton contamination was found to be significant during conjunction: the E1-E2-E3 and P2-P3 trends were very similar and overall of the same order of magnitude. Therefore, the proton contamination removal performed through Peck et al. (2015) may be subject to a considerable uncertainty, and the electron observations at E1, E2, and E3 may not be reliable. Hence, the electron observations in the E1, E2, and E3 energy channels are not shown in Figure 6. Isolated proton precipitation was clear for MetOp-01 and NOAA-15, while precipitation persisted for a wider L shell range for MetOp-02 and NOAA-16. NOAA-15 shows a very interesting precipitation pattern with double precipitation signatures for protons occurring at 13:20:30 UT and then again at 13:21 UT, extending for ~ 40 s. However, the trapped flux for E4 (E_{40}) was at background level, similar to the precipitating flux (E_{40}), narrowing the precipitation width to $\Delta L \sim 0.2$. Such low flux level is reasonable considering the fact that NOAA-15 precipitation occurred 2 hr later than the first precipitation event

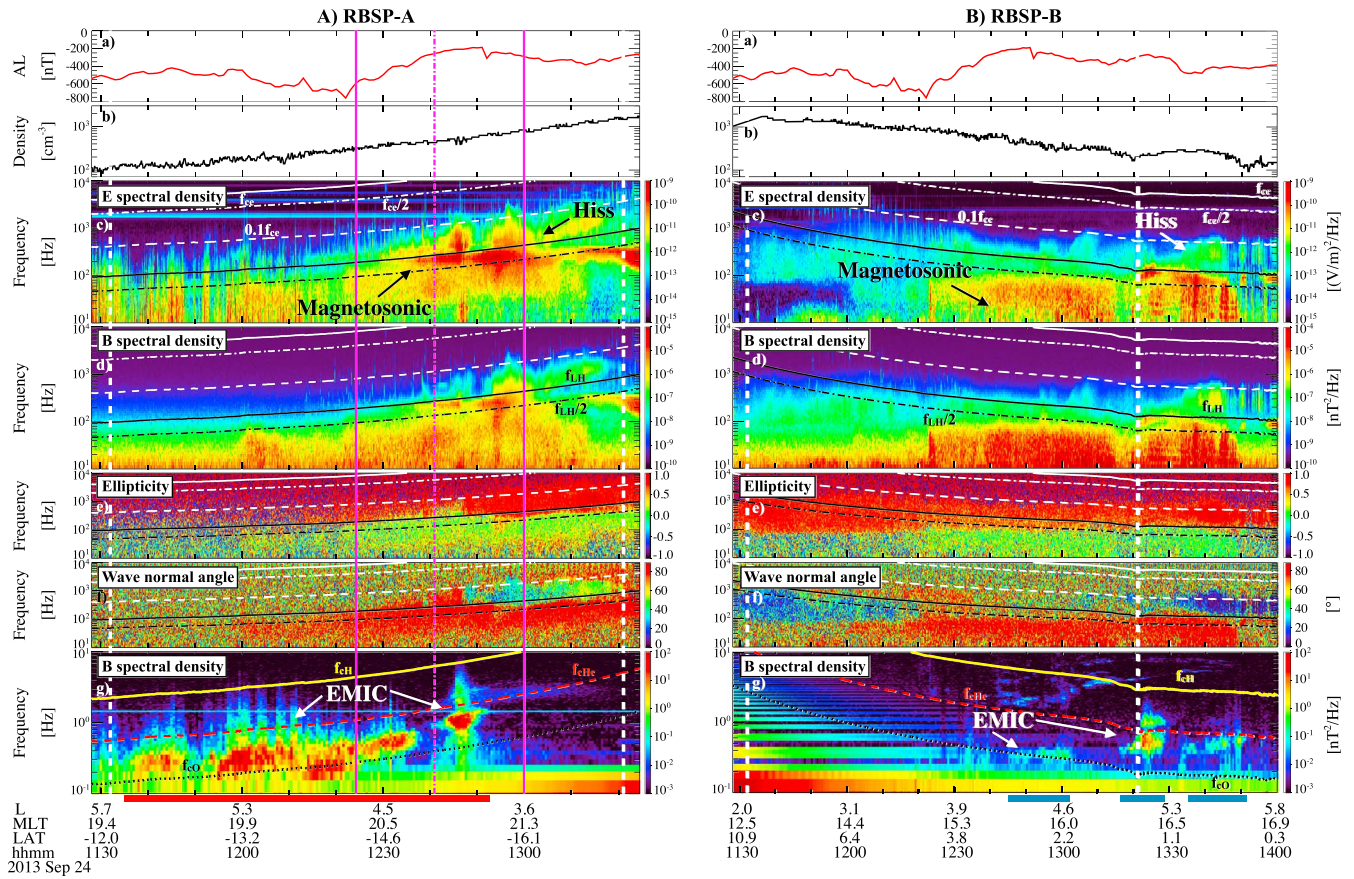


Figure 5. Observations from RBSP-A (A) and RBSP-B (B) on 24 September 2013 with the same format as in Figure 1. The bars at the bottom show the UT time of EMIC wave activity marked with thick lines along the RBSP trajectory in Figure 6 (red for RBSP-A; light blue for RBSP-B). EMIC = electromagnetic ion cyclotron; RBSP = Radiation Belt Storm Probes; MLT = magnetic local time.

(NOAA-16): persistent REP likely has depleted the trapped electron population, as shown in the phase space density (PSD) analysis in Capannolo et al. (2018).

Figure 6E summarizes the precipitation events in the L-MLT polar plot, displaying the trajectories of the POES satellites during the observed precipitation (gray shaded areas in Figures 6A–6D), as well as RBSP-A (red, inbound) and RBSP-B (blue, outbound). All electron precipitation events occurred in the high-density region inside the plasmasphere, as can be inferred from the in situ density measurement of RBSP-A (Figure 5Ab) and RBSP-B (Figure 5Bb). This case study shows a wide precipitation range in L shell. The precipitation on the nightside (MetOp-01, MetOp-02, and NOAA-16) covered $\Delta L \sim 0.4$ – 0.5 . Such observations suggest that favorable conditions for EMIC-driven scattering occurred in localized regions, but with a larger extent than what was observed in the above two events. Simultaneous proton and electron precipitation indeed was observed from 11:32 UT (detected by NOAA-16) to 13:21 UT (observed by NOAA-15), at multiple locations over 16.3–20.4 MLT and 3.7–4.7 L shell.

4. Quasi-Linear Theory Comparison

We use quasi-linear theory (Ni et al., 2015; Summers, 2005) to estimate the efficiency of the observed waves in scattering electrons into the loss cone. The calculations are based on the wave spectra and plasma parameters measured by RBSP around the UT of conjunction with POES, and provide the pitch angle diffusion coefficients due to resonant interactions. We use the latitudinally varying model of wave normal angles in Ni et al. (2015) and assume a cold ion population of 70% H⁺, 20% He⁺, and 10% O⁺ (Lee & Angelopoulos, 2014;

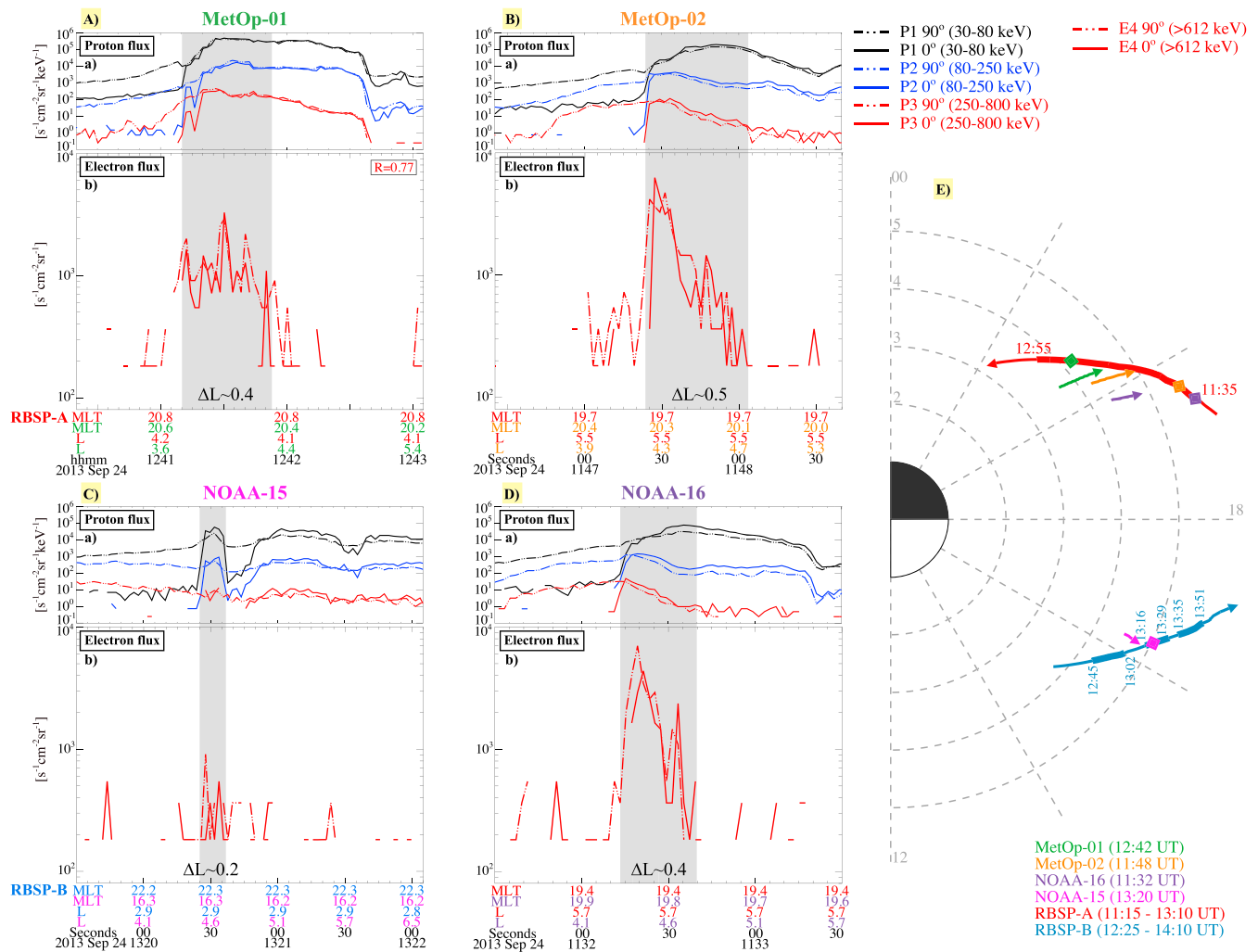


Figure 6. An overview of particle precipitation observed on 24 September 2013 from MetOp-01 (A), MetOp-02 (B), NOAA-15 (C), and NOAA-16 (D). (E) L-MLT polar plot with noon to the bottom: MetOp-01, MetOp-02, NOAA-15, and NOAA-16 trajectories during the observed precipitation (gray areas in A–D) are in green, orange, magenta, and purple, respectively; the time stamps in the legend indicate the precipitation UT time for MetOp-01 (green), MetOp-02 (orange), NOAA-15 (magenta), and NOAA-16 (purple); RBSP-A trajectory between 11:15 UT and 13:10 UT is in red, RBSP-B trajectory between 12:25 and 14:10 UT is in light blue, where thicker lines indicate the EMIC wave observations with the starting and ending time marked with the red time stamps. The RBSP-A location at the UT time of observed precipitation for MetOp-01, MetOp-02, and NOAA-16 is indicated with a green, an orange, and a purple diamond, respectively. The purple diamond on top of RBSP-B trajectory indicates the location at the UT time of the precipitation observed by NOAA-15. MetOp = Meteorological Operational satellite programme; NOAA = National Oceanic and Atmospheric Administration; MLT = magnetic local time; RBSP = Radiation Belt Storm Probes.

Meredith et al., 2014). The resonance numbers include the Landau resonance and span from -5 to 5 . For the H-band EMIC waves, the lower and upper frequency cutoffs used are $0.26 f_{\text{CH}}$ and $0.99 f_{\text{CH}}$, respectively. The same normalized values were used for the He-band EMIC waves ($0.26 f_{\text{CHe}}$ and $0.99 f_{\text{CHe}}$). The diffusion coefficients are shown in Figures 7a–7d for the 10 September 2015 event and in Figures 8a–8d for the 28 February 2015 event.

In order to quantify the electron precipitation driven by the observed waves, we calculate the total diffusion coefficients (from EMIC, hiss, and magnetosonic waves). Due to pitch angle scattering, the electron flux decays exponentially but preserves its pitch angle distribution as a function of pitch angle (Ni et al., 2013; O'Brien et al., 2014). Hence, we use the quasi-equilibrium state formulae by Theodoridis and Paolini (1967) to calculate the normalized equatorial electron pitch angle distribution. Figures 7e and 8e show the equatorial electron flux (normalized to that at 90° equatorial pitch angle) as a function of equatorial pitch angle, color coded by energy, respectively for 10 September 2015 and 28 February 2015. The dashed vertical lines indicate the equatorial bounce loss cone at the L value during conjunction ($L \sim 4.1$ for Case 1, $L \sim 3.8$ for

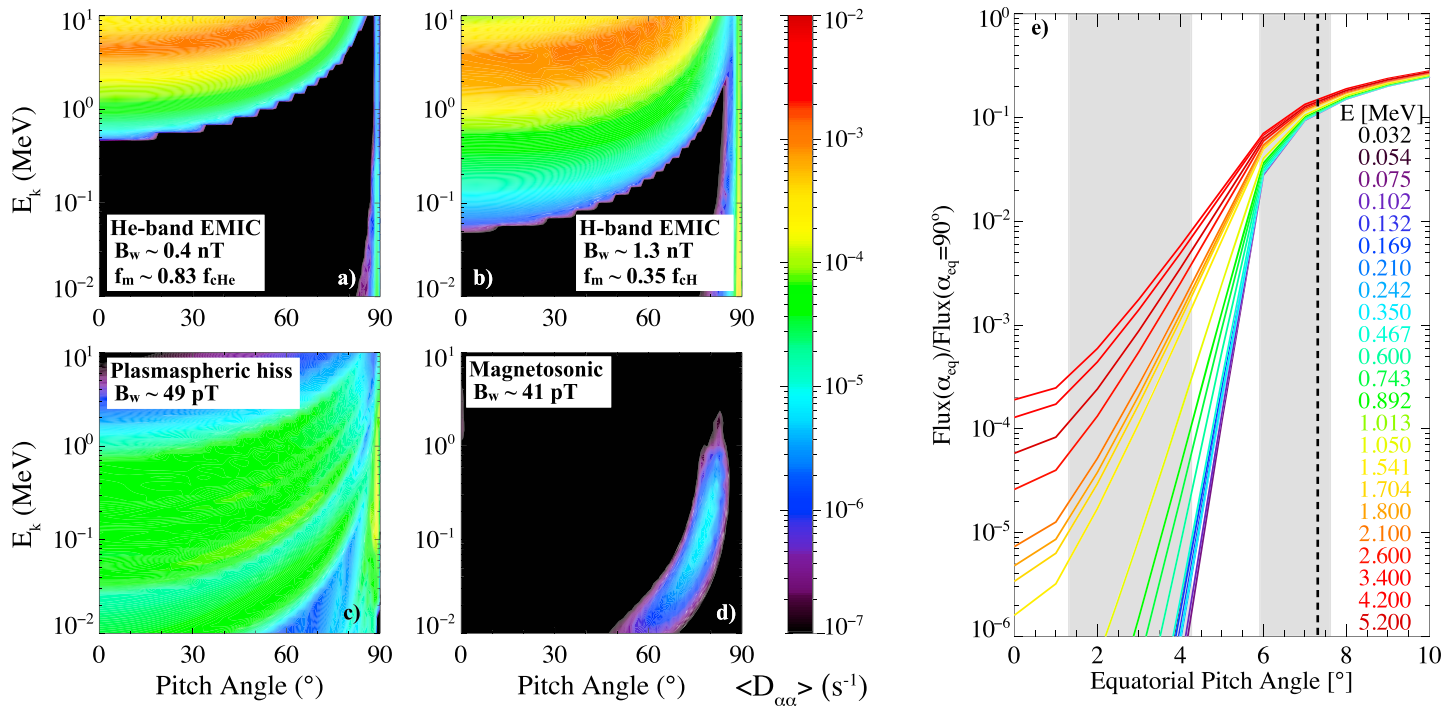


Figure 7. Quasi-linear estimates of electron pitch angle scattering driven by various magnetospheric waves for the event of 10 September 2015, during RBSP-A/NOAA-15 conjunction. (a) Drift and bounce averaged pitch angle diffusion coefficients in per second as a function of pitch angle and energy for He-band EMIC waves, (b) H-band EMIC waves, (c) plasmaspheric hiss, and (d) magnetosonic waves. B_w is the root-mean-square wave amplitude, and f_m is the central frequency of the EMIC wave spectra. (e) Normalized electron flux as a function of equatorial pitch angle, color coded by energy in MeV: The dashed vertical line indicates the equatorial bounce loss cone angle at $L = 4.1$ (at closest conjunction), and gray areas indicate the pitch angle ranges for the 0° (left) and 90° telescope (right) obtained considering a 15° half-angle field of view, during conjunction in Figure 1A. EMIC = electromagnetic ion cyclotron.

Case 2). We show with gray shaded regions the ranges of equatorial pitch angles measured by the 0° and 90° telescopes, given their full field of view of 30°.

It is worthwhile to note that for the 24 September 2013 event (Case study 3), the quasi-linear theory comparison is already discussed in Capannolo et al. (2018), and thus, we only briefly describe the major findings as follows. The comparison of quasi-linear pitch angle diffusion coefficients of He-band and H-band EMIC waves, plasmaspheric hiss, and magnetosonic waves shows that EMIC waves (particularly the He-band) led to the most effective pitch angle scattering of high-energy electrons (greater than a few MeV). The trend of the estimated electron precipitation at various energies is overall in agreement with the strong precipitation at relativistic energy ranges observed by MetOp-01.

4.1. Case Study 1: 10 September 2015

Figures 7a–7d show the pitch angle diffusion coefficients from the wave spectra measured by RBSP-A averaged over a 5-min interval centered at 20:07 UT. In this time interval, density is $\sim 180 \text{ cm}^{-3}$, and the ratio of plasma to electron cyclotron frequency (f_{pe}/f_{ce}) is 11.1. The He-band EMIC waves ($B_w \sim 0.4$ nT) are weaker than the H-band EMIC waves ($B_w \sim 1.3$ nT); however, the diffusion coefficients are comparable and lead to scattering of electrons into the loss cone on timescales of ~ 10 min. Only electrons with low-intermediate pitch angles and relativistic energies are scattered by EMIC waves through cyclotron resonance, consistently with previous studies (Usanova et al., 2014; Zhang et al., 2016). The calculated minimum resonant energy for the EMIC waves can extend down to hundreds of keV; however, the timescales at such energy values are very long (approximately a day). The diffusion coefficients for plasmaspheric hiss (Figure 7c, $B_w \sim 49$ pT) are dominant up to ~ 1 MeV, but the associated shortest pitch angle scattering timescale is ~ 1.4 hr. Magnetosonic waves (Figure 7d, $B_w \sim 41$ pT) have very weak diffusion coefficients at high pitch angles ($>60^\circ$) and thus do not contribute to the precipitation of electrons.

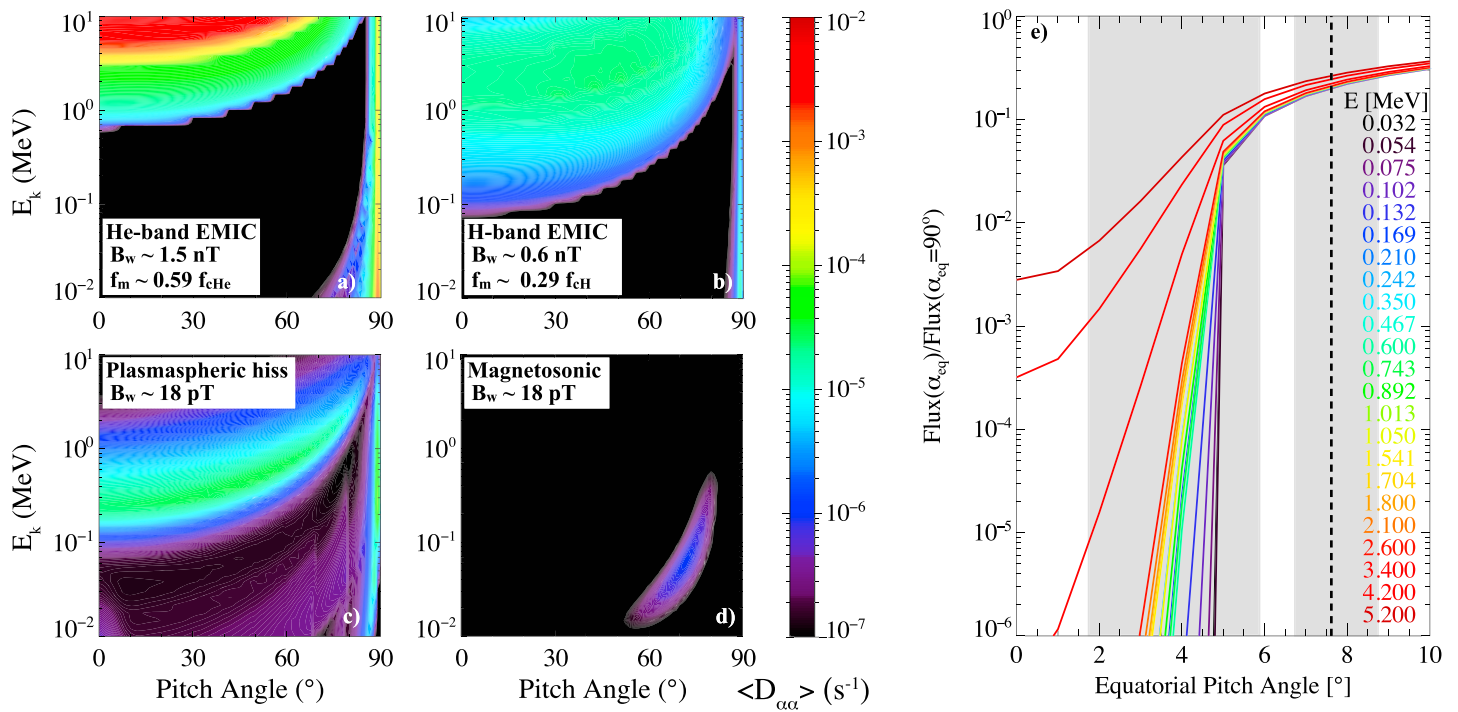


Figure 8. Quasi-linear results for 28 February 2015, during RBSP-A/MetOp-01 conjunction (similar format to Figure 7). The dashed vertical line indicates the equatorial bounce loss cone angle at $L = 3.8$. EMIC = electromagnetic ion cyclotron.

Figure 7e shows the normalized pitch angle distribution within 10° of equatorial pitch angle. The loss cone (gray area to the left of the vertical dashed line) tends to become more filled with increasing energy: hundreds of keV electrons show a much lower normalized flux than that of >1 -MeV electrons. As expected, EMIC waves are more efficient in scattering higher-energy electrons into the loss cone than lower energy ones. In addition, the normalized flux at 5.2 MeV is lower than that at 3.4 and 4.2 MeV, which agrees with the He-band EMIC wave diffusion coefficient profile, peaking at ~ 4 MeV. This result overall agrees with the high precipitating-to-trapped ratio measured by both NOAA-15 and NOAA-18 satellites during the precipitation shown in Figures 2A and 2B: the ratios in E2 and E3 channels are on average 0.05, whereas the one in E4 is ~ 0.4 . Note that a one-to-one comparison between the theoretical and observed ratio is difficult because the NOAA electron channels are integrated over a large range of energies. Nevertheless, the trend of strong precipitation at relativistic energies but not at low energies is consistent with the NOAA observations.

4.2. Case Study 2: 28 February 2015

The pitch angle diffusion coefficients in Figures 8a–8d are calculated using quasi-linear theory based on the RBSP-A wave observations averaged over 20:32–20:36 UT, in conjunction with MetOp-01 observations of electron precipitation. Note that for the proximity in L and MLT between these waves and MetOp-02 location, the quasi-linear results can be compared to MetOp-02 precipitation observations as well. The total electron density in this event is $\sim 90 \text{ cm}^{-3}$ and f_{pe}/f_{ce} ratio is 9.3. He-band EMIC waves dominate the pitch angle scattering, given their high amplitude of 1.5 nT. They precipitate >5 MeV electrons at low-intermediate pitch angles on timescales of ~ 5 min. H-band EMIC waves were weaker ($B_w \sim 0.6$ nT) and did not contribute much to the pitch angle scattering, similarly to plasmaspheric hiss ($B_w \sim 18$ pT) and magnetosonic waves ($B_w \sim 18$ pT). As for the 10 September 2015 event (Case 1), the minimum resonant energy for EMIC waves can extend down to hundreds of keV, but the timescales at these energies are too long to lead to efficient electron precipitation. By comparing the diffusion coefficients of EMIC waves between Case 1 and Case 2, a stronger EMIC wave activity (H-band for Case 1, He-band for Case 2) causes faster pitch angle scattering than a weaker EMIC wave. In addition, in agreement with theory, EMIC waves with center frequencies closer to the ion gyrofrequency lead to lower minimum resonant energy.

Figure 8e shows the normalized flux as a function of equatorial pitch angle, derived from the diffusion coefficients on the left. As for the previous case, the loss cone fills up more as energy increases, showing that EMIC waves are more efficient in scattering higher-energy electrons. As a result of the intense observed He-band EMIC waves, the loss cone is more filled than that in Case 1 and the theoretical precipitating-to-trapped ratio is larger. POES E3 observations in Figures 4B–4D suggest that electron precipitation extended to energies as low as ~ 300 keV, which cannot be explained by the quasi-linear theory. However, the precipitation-to-trapped ratio in the E4 channel is stronger than that in the E3 channel, in agreement with an increasing precipitating-to-trapped ratio estimated from theory.

5. Summary and Discussion

In this paper, we show three case studies of precipitation events observed by multiple low-orbit satellites simultaneously with EMIC wave activity observed in the equatorial magnetosphere and/or at the ground by magnetometers (15 September 2015, 28 February 2015, and 24 September 2013). Coordinated multisatellite measurements allow us to explore the minimum L shell extent of the proton and electron precipitation at various energies, as well as their durations. We also performed quasi-linear simulations to compare the scattering efficiency of the EMIC, hiss and magnetosonic waves to the observed electron precipitation.

All the cases occurred during substorms, within the plasmasphere (at least during the periods when RBSP density measurements were available) and near the dusk sector, in agreement with previous studies (Shekhar et al., 2018; Yahnin et al., 2017), given the favorable region of EMIC wave excitation due to ring current proton injections (Jordanova et al., 2008). The precipitation trends at low orbit all show strong precipitation of both ring current protons and relativistic electrons (E4 channel onboard POES/MetOp), with precipitation patterns very similar across all the available LEO satellites located near the conjugate locations of the EMIC wave activity observed by RBSP.

In the 10 September 2015 case study, simultaneous precipitation of protons and relativistic electrons was observed by two LEO satellites in conjunction with EMIC waves measured by RBSP-A. Within a 15-min window, both NOAA-15 and NOAA-18 observed a very similar electron and proton precipitation patterns at ~ 18 MLT with an L shell extent of ~ 0.3 for NOAA-15 and ~ 0.2 for NOAA-18.

Similar patterns of electron precipitation were also observed by four LEO spacecraft (MetOp-01, MetOp-02, NOAA-15, and NOAA-19) over 20:14–20:55 UT on 28 February 2015. Electron precipitation was clearly observed in the E4 channel (>612 keV) and also extended into the E3 channel (>287 keV), simultaneously with proton precipitation. For this case study, satellites that observed precipitation were located in a ~ 4 hr MLT and ~ 1.4 L shell range in the dusk sector. In support of such large precipitation extent, EMIC wave activity was detected during the outbound RBSP-A orbit and also at multiple stations at the ground, covering the L-MLT ranges that consistently map to the POES locations. The precipitation width observed at each satellite, instead, seems to be more localized in L shell for the postdusk events ($\Delta L \sim 0.1$ – 0.2) and slightly more extended for those in the predusk sector ($\Delta L \sim 0.3$ – 0.4). An explanation for this is likely found in the different locations of the precipitation events: the postdusk events differ from the pre-dusk ones by ~ 4 hr in MLT, and it is very likely that the EMIC wave spectra and local plasma conditions driving precipitation were different at these two locations.

The 24 September 2013 case study also consists of four LEO satellites (MetOp-01, MetOp-02, NOAA-15, and NOAA-16) detecting electron precipitation at different locations within ~ 2 hr UT (11:32–13:21 UT), ~ 1 L shell (3.7–4.7) and ~ 4.1 hr in MLT (16.3–20.4). EMIC waves were observed by both RBSP-A and RBSP-B at locations that map consistently with the precipitation location observed by POES but likely drive two different proton and electron precipitations over the predusk and postdusk sectors. Moreover, the precipitation extent at each spacecraft near the postdusk sector is the largest among the three case studies ($\Delta L \sim 0.4$ – 0.5), whereas the observed precipitation near the pre-dusk sector spanned only $\Delta L \sim 0.2$ due to electron population depletion.

Overall, an interesting feature observed in all of the above three case studies is that each single precipitation event detected by one LEO spacecraft is rather latitudinally localized (average $\Delta L \sim 0.3$), suggesting that EMIC waves may efficiently pitch angle scatter electrons only in a localized region, likely where resonance conditions are more favorable. Such a localized feature of REP events was observed in the statistical study by

Shekhar et al. (2017) and mentioned in Engebretson et al. (2018) as well and agrees with EMIC waves mainly occurring in localized L shells (Blum et al., 2016; Blum et al., 2017). The limited EMIC-driven scattering can also be seen in the time evolution of PSD profiles (e.g., Capannolo et al., 2018; Shprits et al., 2017; Su et al., 2016), where radiation belt dropouts (PSD minima) associated with EMIC waves occur only at localized L^* ranges.

However, due to either temporal evolution of the waves or the different characteristics of the EMIC wave properties in the magnetosphere, signatures of strong precipitation can also occur at various L shells and MLTs. Using a satellite constellation such as POES/MetOp was very useful to investigate these spatial and temporal phenomena. In this study, we were able to explore the spatial extent of precipitation driven by EMIC waves and found that precipitation can occur in different locations within a rather broad L -MLT region (up to ~ 1.4 L shells and ~ 4.4 hr MLT), consistent with the statistical results by Shekhar et al. (2017). For our cases, the EMIC waves observed at widely different L and MLT locations (Case studies 2 and 3) might not be necessarily correlated but can clearly still drive efficient proton and electron precipitation in the nearby regions, as detected by POES/MetOp. It is important to note that the precipitation extent in L shell and MLT, as well as its duration reported in this paper, are only a lower limit, due to the limited availability of the POES satellites in the region of interest. In reality, such precipitation could potentially extend beyond the identified region in this paper.

As for the energy of electrons precipitating in the upper atmosphere, the 10 September 2015 case corresponds to the traditional precipitation of relativistic electrons driven by EMIC waves occurring only in the relativistic electron channel (Ni et al., 2015). These observations are consistent with the results of quasi-linear theory shown in this study. Since the EMIC waves in the intervals of study are the most intense waves, they dominate the pitch angle scattering and lead to a normalized pitch angle distribution with a loss cone that fills up as the electron energy increases, confirming that EMIC waves are most efficient in scattering >1 -MeV electrons into the upper atmosphere. The 24 September 2013 case also showed clear electron precipitation at relativistic energy, which is consistent with the quasi-linear estimate (shown in Capannolo et al., 2018), granting it is not entirely clear whether such electron precipitation extended to even lower energies due to the possible proton contamination in the low-energy electron channels even after removing the contamination following Peck et al. (2015). Interestingly, the 28 February 2015 case also showed unexpected precipitation at lower energy (E3, >287 keV). Such a feature is significantly underestimated by the quasi-linear theory, suggesting that the assumptions used in the diffusion approach might not be suitable to explain the interaction between EMIC waves and lower-energy electrons. On the other hand, the theoretical work by Chen et al. (2016) demonstrated that EMIC waves can potentially scatter electrons down to hundreds of keV via nonresonant interactions, which may explain the significant percentage of precipitation events with the energy peak at ~ 300 keV observed in the statistical study by Hendry et al. (2017).

In summary, our findings provide clear evidence that, although precipitation events driven by EMIC waves span a narrow L shell extent (on average $\Delta L \sim 0.3$), they are triggered in various locations, likely within a rather wide region of L shells and MLT sectors and still maintaining an overall similar pattern of precipitation. Such results could further explain why electron precipitation is localized, but still potentially lead to electron dropouts in the outer radiation belt.

Coordinated multisatellite measurements in the equatorial magnetosphere, at low orbit and at ground allow us to identify the drivers of particle precipitation and determine the spatial extent (in L shell) where particle precipitation occurs. The cases shown in the present study are just a few fortuitous conjunction events between the Van Allen Probes and the POES/MetOp constellation. However, there are several other magnetospheric spacecraft (e.g., MMS, THEMIS, Arase, and Cluster), LEO satellites, as well as existing (FIREBIRD, AC6, ELFEN, etc.) and future CubeSats that can be used to provide a more comprehensive understanding of particle precipitation. For example, the minimum energy of precipitating electrons driven by EMIC waves is still under debate and the improved resolution in energy and pitch angle from new CubeSats will potentially provide insightful observational evidence. It would also be interesting to understand if the recently identified latitudinal dependence of fine-structured EMIC waves (Matsuda et al., 2018) drives different patterns of particle precipitation. These interesting investigations are beyond the scope of the present study, and thus left as future work.

Acknowledgments

This research is supported by NSF grant AGS-1723588, AFOSR grant FA9550-15-1-0158, and the Alfred P. Sloan Research Fellowship FG-2018-10936. Work at Augsburg University was supported by NSF grant AGS-1651263. The work at the University of Iowa was performed under the support of JHU/APL contract 921647 under NASA Prime contract NAS5-01072. The authors Capannolo L. and Li W. would like to acknowledge Aaron Hendry for the useful discussion on proton contaminations of POES/MetOp data. The Van Allen probes data from the EMFISIS instrument suite were obtained from <http://emfisis.physics.uiowa.edu/Flight/> website, and data from the ECT instrument were obtained from http://www.rbsp-ect.lanl.gov/data_pub/ website. The POES and MetOp data were obtained from <https://www.ngdc.noaa.gov/stp/satellite/poes/> website. We acknowledge the World Data Center for Geomagnetism, Kyoto for providing AE, AL, and Dst indices (<http://wdc.kugi.kyoto-u.ac.jp/kp/index.html>). We acknowledge Jennifer Posch for providing the data of Halley, accessible at <http://space.augsburg.edu/searchcoil/index.html> website. The search coil magnetometer at Halley Station is operated by the British Antarctic Survey. Data from CARISMA/ISLL was downloaded at the website (http://www.carisma.ca/themis_carisma_cdf). We acknowledge the Sodankylä Geophysical Observatory (SGO), University of Oulu, for providing the OUL station data (<http://www.sgo.fi/Data/Pulsation/>).

References

- Allen, R. C., Zhang, J.-C., Kistler, L. M., Spence, H. E., Lin, R.-L., Klecker, B., et al. (2016). A statistical study of EMIC waves observed by Cluster: 2. Associated plasma conditions. *Journal of Geophysical Research: Space Physics*, 121, 6458–6479. <https://doi.org/10.1002/2016JA022541>
- Asikainen, T., Mursula, K., & Maliniemi, V. (2012). Correction of detector noise and recalibration of NOAA/MEPED energetic proton fluxes. *Journal of Geophysical Research*, 117, A09204. <https://doi.org/10.1029/2012JA017593>
- Blum, L. W., Agapitov, O., Bonnell, J. W., Kletzing, C., & Wygant, J. (2016). EMIC wave spatial and coherence scales as determined from multipoint Van Allen Probe measurements. *Geophysical Research Letters*, 43, 4799–4807. <https://doi.org/10.1002/2016GL068799>
- Blum, L. W., Bonnell, J. W., Agapitov, O., Paulson, K., & Kletzing, C. (2017). EMIC wave scale size in the inner magnetosphere: Observations from the dual Van Allen Probes. *Geophysical Research Letters*, 44, 1227–1233. <https://doi.org/10.1002/2016GL072316>
- Blum, L. W., Halford, A., Millan, R., Bonnell, J. W., Goldstein, J., Usanova, M., et al. (2015). Observations of coincident EMIC wave activity and duskside energetic electron precipitation on 18–19 January 2013. *Geophysical Research Letters*, 42, 5727–5735. <https://doi.org/10.1002/2015GL065245>
- Cao, X., Ni, B., Liang, J., Xiang, Z., Wang, Q., Shi, R., et al. (2016). Resonant scattering of central plasma sheet protons by multiband EMIC waves and resultant proton loss timescales. *Journal of Geophysical Research: Space Physics*, 121, 1219–1232. <https://doi.org/10.1002/2015JA021933>
- Capannolo, L., Li, W., Ma, Q., Zhang, X.-J., Redmon, R. J., Rodriguez, J. V., et al. (2018). Understanding the driver of energetic electron precipitation using coordinated multisatellite measurements. *Geophysical Research Letters*, 45, 6755–6765. <https://doi.org/10.1029/2018GL078604>
- Carson, B. R., Rodger, C. J., & Clilverd, M. A. (2012). POES satellite observations of EMIC-wave driven relativistic electron precipitation during 1998–2010. *Journal of Geophysical Research*, 118, A02313. <https://doi.org/10.1029/2012JA017998>
- Chen, L., Thorne, R. M., & Bortnik, J. (2011). The controlling effect of ion temperature on EMIC wave excitation and scattering. *Geophysical Research Letters*, 38, L16109. <https://doi.org/10.1029/2011GL048653>
- Chen, L., Thorne, R. M., Bortnik, J., & Zhang, X.-J. (2016). Nonresonant interactions of electromagnetic ion cyclotron waves with relativistic electrons. *Journal of Geophysical Research: Space Physics*, 121, 9913–9925. <https://doi.org/10.1002/2016JA022813>
- Clilverd, M. A., Rodger, C. J., McCarthy, M., Millan, R., Blum, L. W., Cobbett, N., et al. (2017). Investigating energetic electron precipitation through combining ground-based and balloon observations. *Journal of Geophysical Research: Space Physics*, 122, 534–546. <https://doi.org/10.1002/2016JA022812>
- Dubynagin, S., Ganushkina, N. Y., & Sergeev, V. A. (2018). Formation of 30 keV proton isotropic boundaries during geomagnetic storms. *Journal of Geophysical Research: Space Physics*, 123, 3436–3459. <https://doi.org/10.1002/2017JA024587>
- Engebretson, M. J., Lessard, M. R., Bortnik, J., Green, J. C., Horne, R. B., Detrick, D. L., et al. (2008). Pc1–Pc2 waves and energetic particle precipitation during and after magnetic storms: Superposed epoch analysis and case studies. *Journal of Geophysical Research*, 113, A01211. <https://doi.org/10.1029/2007JA012362>
- Engebretson, M. J., Posch, J. L., Braun, D. J., Li, W., Ma, Q., Kellerman, A. C., et al. (2018). EMIC wave events during the four GEM QARB challenge intervals. *Journal of Geophysical Research: Space Physics*, 123, 6394–6423. <https://doi.org/10.1029/2018JA025505>
- Engebretson, M. J., Posch, J. L., Wygant, J. R., Kletzing, C. A., Lessard, M. R., Huang, C. L., et al. (2015). Van Allen probes, NOAA, GOES, and ground observations of an intense EMIC wave event extending over 12 h in magnetic local time. *Journal of Geophysical Research: Space Physics*, 120, 5465–5488. <https://doi.org/10.1002/2015JA021227>
- Erlanson, R. E., & Ukhorskiy, A. J. (2001). Observations of electromagnetic ion cyclotron waves during geomagnetic storms: Wave occurrence and pitch angle scattering. *Journal of Geophysical Research*, 106(A3), 3883–3895. <https://doi.org/10.1029/2000JA000083>
- Evans, D. S., & Greer, M. S. (2004). *Polar Orbiting Environmental Satellite Space Environment Monitor-2: Instrument descriptions and archive data documentation archive data documentation*, NOAA Technical Memorandum 93, Version 1.4. Boulder, CO: Space Weather Predict. Cent.
- Fraser, B. J., Grew, R. S., Morley, S. K., Green, J. C., Singer, H. J., Loto'aniu, T. M., & Thomsen, M. F. (2010). Storm time observations of electromagnetic ion cyclotron waves at geosynchronous orbit: GOES results. *Journal of Geophysical Research*, 115, A05208. <https://doi.org/10.1029/2009JA014516>
- Galand, M., & Evans, D. S. (2000). Radiation damage of the proton MEPED detector on POES (TIROS/NOAA) satellites, Research Gate, <http://www.researchgate.net/publication/268271719>
- Gilson, M. L., Raeder, J., Donovan, E., Ge, Y. S., & Kepko, L. (2012). Global simulation of proton precipitation due to field line curvature during substorms. *Journal of Geophysical Research*, 117, A05216. <https://doi.org/10.1029/2012JA017562>
- Green, J. C. (2013). *MEPED telescope data processing algorithm theoretical basis document*. National Geophysical Data Center, Boulder, Colo: Natl. Oceanic and Atmos. Admin.
- Hendry, A. T., Rodger, C. J., & Clilverd, M. A. (2017). Evidence of sub-MeV EMIC-driven electron precipitation. *Geophysical Research Letters*, 44, 1210–1218. <https://doi.org/10.1002/2016GL071807>
- Hirai, A., Tsuchiya, F., Obara, T., Kasaba, Y., Katoh, Y., Misawa, H., et al. (2018). Temporal and spatial correspondence of Pc1/EMIC waves and relativistic electron precipitations observed with ground-based multi-instruments on 27 March 2017. *Geophysical Research Letters*, 45, 13,182–13,191. <https://doi.org/10.1029/2018GL080126>
- Horne, R. B., & Thorne, R. M. (1998). Potential waves for relativistic electron scattering and stochastic acceleration during magnetic storms. *Geophysical Research Letters*, 25(15), 3011–3014. <https://doi.org/10.1029/98GL01002>
- Horne, R. B., Thorne, R. M., Glauert, S. A., Meredith, N. P., Pokhotelov, D., & Santolík, O. (2007). Electron acceleration in the Van Allen radiation belts by fast magnetosonic waves. *Geophysical Research Letters*, 34, L17107. <https://doi.org/10.1029/2007GL030267>
- Hudson, M. K., Baker, D. N., Goldstein, J., Kress, B. T., Paral, J., Toffoletto, F. R., & Wiltberger, M. (2014). Simulated magnetopause losses and Van Allen Probe flux dropouts. *Geophysical Research Letters*, 41, 1113–1118. <https://doi.org/10.1002/2014GL059222>
- Jordanova, V. K., Albert, J., & Miyoshi, Y. (2008). Relativistic electron precipitation by EMIC waves from self-consistent global simulations. *Journal of Geophysical Research*, 113, A00A10. <https://doi.org/10.1029/2008JA013239>
- Kersten, T., Horne, R. B., Glauert, S. A., Meredith, N. P., Fraser, B. J., & Grew, R. S. (2014). Electron losses from the radiation belts caused by EMIC waves. *Journal of Geophysical Research: Space Physics*, 119, 8820–8837. <https://doi.org/10.1002/2014JA020366>
- Kim, H., Lessard, M. R., Engebretson, M. J., & Lühr, H. (2010). Ducting characteristics of pc 1 waves at high latitudes on the ground and in space. *Journal of Geophysical Research*, 115, A09310. <https://doi.org/10.1029/2010JA015323>

- Kletzing, C. A., Kurth, W. S., Acuna, M., MacDowall, R. J., Torbert, R. B., Averkamp, T., et al. (2013). The Electric and Magnetic Field Instrument Suite and Integrated Science (EMFISIS) on RBSP. *Space Science Reviews*, 179(1-4), 127–181. <https://doi.org/10.1007/s11214-013-9993-6>
- Kurth, W. S., De Pascuale, S., Faden, J. B., Kletzing, C. A., Hospodarsky, G. B., Thaller, S., & Wygant, J. R. (2015). Electron densities inferred from plasma wave spectra obtained by the waves instrument on Van Allen Probes. *Journal of Geophysical Research: Space Physics*, 120, 904–914. <https://doi.org/10.1002/2014JA020857>
- Lee, J. H., & Angelopoulos, V. (2014). On the presence and properties of cold ions near Earth's equatorial magnetosphere. *Journal of Geophysical Research: Space Physics*, 119, 1749–1770. <https://doi.org/10.1002/2013JA019305>
- Li, W., Shprits, Y. Y., & Thorne, R. M. (2007). Dynamic evolution of energetic outer zone electrons due to wave-particle interactions during storms. *Journal of Geophysical Research*, 112, A10220. <https://doi.org/10.1029/2007JA012368>
- Li, W., Thorne, R. M., Ma, Q., Ni, B., Bortnik, J., Baker, D. N., et al. (2014). Radiation belt electron acceleration by chorus waves during the 17 March 2013 storm. *Journal of Geophysical Research: Space Physics*, 119, 4681–4693. <https://doi.org/10.1002/2014JA019945>
- Li, Z., Millan, R. M., Hudson, M. K., Woodger, L. A., Smith, D. M., Chen, Y., et al. (2014). Investigation of EMIC wave scattering as the cause for the BARREL 17 January 2013 relativistic electron precipitation event: A quantitative comparison of simulation with observations. *Geophysical Research Letters*, 41, 8722–8729. <https://doi.org/10.1002/2014GL062273>
- Lyons, L. R., & Evans, D. S. (1984). An association between discrete aurora and energetic particle boundaries. *Journal of Geophysical Research*, 89(A4), 2395–2400. <https://doi.org/10.1029/JA089iA04p02395>
- Ma, Q., Li, W., Thorne, R. M., Bortnik, J., Kletzing, C. A., Kurth, W. S., & Hospodarsky, G. B. (2016). Electron scattering by magnetosonic waves in the inner magnetosphere. *Journal of Geophysical Research: Space Physics*, 121, 274–285. <https://doi.org/10.1002/2015JA021992>
- Matsuda, S., Kasahara, Y., Miyoshi, Y., Nomura, R., Shoji, M., Matsuoka, A., et al. (2018). Spatial distribution of fine-structured and unstructured EMIC waves observed by the Arase satellite. *Geophysical Research Letters*, 45, 11,530–11,538. <https://doi.org/10.1029/2018GL080109>
- Mauk, B. H., Fox, N. J., Kanekal, S. G., Kessel, R. L., Sibeck, D. G., & Ukhorskiy, A. (2013). Science objectives and rationale for the Radiation Belt Storm Probes Mission. *Space Science Reviews*, 179(1-4), 3–27. <https://doi.org/10.1007/s11214-012-9908-y>
- Meraner, K., & Schmidt, H. (2018). Climate impact of idealized winter polar mesospheric and stratospheric ozone losses as caused by energetic particle precipitation. *Atmospheric Chemistry and Physics*, 18(2), 1079–1089. <https://doi.org/10.5194/acp-18-1079-2018>
- Meredith, N. P., Horne, R. B., Kersten, T., Fraser, B. J., & Grew, R. S. (2014). Global morphology and spectral properties of EMIC waves derived from CRRES observations. *Journal of Geophysical Research: Space Physics*, 119, 5328–5342. <https://doi.org/10.1002/2014JA020064>
- Millan, R. M., McCarthy, M. P., Sample, J. G., Smith, D. M., Thompson, L. D., McGaw, D. G., et al. (2013). The Balloon Array for RBSP Relativistic Electron Losses (BARREL). *Space Science Reviews*, 179(1-4), 503–530. <https://doi.org/10.1007/s11214-013-9971-z>
- Millan, R. M., & Thorne, R. M. (2007). Review of radiation belt relativistic electron losses. *Journal of Atmospheric and Solar - Terrestrial Physics*, 69(3), 362–377. <https://doi.org/10.1016/j.jastp.2006.06.019>
- Min, K., Lee, J., Keika, K., & Li, W. (2012). Global distribution of EMIC waves derived from THEMIS observations. *Journal of Geophysical Research*, 117, A05219. <https://doi.org/10.1029/2012JA017515>
- Mironova, I. A., Aplin, K. L., Arnold, F., Bazilevskaya, G. A., Harrison, R. G., Krivolutsky, A. A., et al. (2015). Energetic particle influence on the Earth's atmosphere. *Space Science Reviews*, 194(1-4), 1–96. <https://doi.org/10.1007/s11214-015-0185-4>
- Miyoshi, Y., Sakaguchi, K., Shiohara, K., Evans, D., Albert, J., Connors, M., & Jordanova, V. (2008). Precipitation of radiation belt electrons by EMIC waves, observed from ground and space. *Geophysical Research Letters*, 35, L23101. <https://doi.org/10.1029/2008GL035727>
- Morley, S. K., Ables, S. T., Sciffer, M. D., & Fraser, B. J. (2009). Multipoint observations of Pc1-2 waves in the afternoon sector. *Journal of Geophysical Research*, 114, A09205. <https://doi.org/10.1029/2009JA014162>
- Ni, B., Bortnik, J., Thorne, R. M., Ma, Q., & Chen, L. (2013). Resonant scattering and resultant pitch angle evolution of relativistic electrons by plasmaspheric hiss. *Journal of Geophysical Research: Space Physics*, 118, 7740–7751. <https://doi.org/10.1002/2013JA019260>
- Ni, B., Cao, X., Zou, Z., Zhou, C., Gu, X., Bortnik, J., et al. (2015). Resonant scattering of outer zone relativistic electrons by multiband EMIC waves and resultant electron loss time scales. *Journal of Geophysical Research: Space Physics*, 120, 7357–7373. <https://doi.org/10.1002/2015JA021466>
- O'Brien, T. P., Claudepierre, S. G., Blake, J. B., Fennell, J. F., Clemmons, J. H., Roeder, J. L., et al. (2014). An empirically observed pitch-angle diffusion eigenmode in the Earth's electron belt near $L^* = 5.0$. *Geophysical Research Letters*, 41, 251–258. <https://doi.org/10.1002/2013GL058713>
- Peck, E. D., Randall, C. E., Green, J. C., Rodriguez, J. V., & Rodger, C. J. (2015). POES MEPED differential flux retrievals and electron channel contamination correction. *Journal of Geophysical Research: Space Physics*, 120, 4596–4612. <https://doi.org/10.1002/2014JA020817>
- Pickett, J. S., Grison, B., Omura, Y., Engebretson, M. J., Dandouras, I., Masson, A., et al. (2010). Cluster observations of EMIC triggered emissions in association with Pc1 waves near Earth's plasmapause. *Geophysical Research Letters*, 37, L09104. <https://doi.org/10.1029/2010GL042648>
- Qin, M., Hudson, M., Millan, R., Woodger, L., & Shekhar, S. (2018). Statistical investigation of the efficiency of EMIC waves in precipitating relativistic electrons. *Journal of Geophysical Research: Space Physics*, 123, 6223–6230. <https://doi.org/10.1029/2018JA025419>
- Reeves, G. D., McAdams, K. L., Friedel, R. H. W., & O'Brien, T. P. (2003). Acceleration and loss of relativistic electrons during geomagnetic storms. *Geophysical Research Letters*, 30(10), 1529. <https://doi.org/10.1029/2002GL016513>
- Rodger, C. J., Clilverd, M. A., Green, J. C., & Lam, M. M. (2010). Use of POES SEM-2 observations to examine radiation belt dynamics and energetic electron precipitation into the atmosphere. *Journal of Geophysical Research*, 115, A04202. <https://doi.org/10.1029/2008JA014023>
- Sandanger, M. I., Ødegaard, L.-K. G., Nesse Tysøy, H., Stadsnes, J., Sørås, F., Oksavik, K., & Aarsnes, K. (2015). In-flight calibration of NOAA POES proton detectors-Derivation of the MEPED correction factors. *Journal of Geophysical Research: Space Physics*, 120, 9578–9593. <https://doi.org/10.1002/2015JA021388>
- Shekhar, S., Millan, R., & Smith, D. (2017). A statistical study of the spatial extent of relativistic electron precipitation with polar orbiting environmental satellites. *Journal of Geophysical Research: Space Physics*, 122, 11,274–11,284. <https://doi.org/10.1002/2017JA024716>
- Shekhar, S., Millan, R. M., & Hudson, M. K. (2018). A statistical study of spatial variation of relativistic electron precipitation energy spectra with Polar Operational Environmental Satellites. *Journal of Geophysical Research: Space Physics*, 123, 3349–3359. <https://doi.org/10.1002/2017JA025041>
- Shprits, Y. Y., Kellerman, A., Aseev, N., Drozdov, A. Y., & Michaelis, I. (2017). Multi-MeV electron loss in the heart of the radiation belts. *Geophysical Research Letters*, 44, 1204–1209. <https://doi.org/10.1002/2016GL072258>

- Silin, I., Mann, I. R., Sydora, R. D., Summers, D., & Mace, R. L. (2011). Warm plasma effects on electromagnetic ion cyclotron wave MeV electron interactions in the magnetosphere. *Journal of Geophysical Research*, 116, A05215. <https://doi.org/10.1029/2010JA016398>
- Sinnhuber, M., Nieder, H., & Wieters, N. (2012). Energetic particle precipitation and the chemistry of the mesosphere/lower thermosphere. *Surveys in Geophysics*, 33(6), 1281–1334. <https://doi.org/10.1007/s10712-012-9201-3>
- Spence, H. E., Reeves, G. D., Baker, D. N., Blake, J. B., Bolton, M., Bourdarie, S., et al. (2013). Science Goals and Overview of the Radiation Belt Storm Probes (RBSP) Energetic Particle, Composition, and Thermal Plasma (ECT) Suite on NASA's Van Allen Probes Mission. *Space Science Reviews*. https://doi.org/10.1007/978-1-4899-7433-4_10
- Su, Z., Gao, Z., Zhu, H., Li, W., Zheng, H., Wang, Y., et al. (2016). Nonstorm time dropout of radiation belt electron fluxes on 24 September 2013. *Journal of Geophysical Research: Space Physics*, 121, 6400–6416. <https://doi.org/10.1002/2016JA022546>
- Summers, D. (2005). Quasi-linear diffusion coefficients for field-aligned electromagnetic waves with applications to the magnetosphere. *Journal of Geophysics Research*, 110, A08213. <https://doi.org/10.1029/2005JA011159>
- Summers, D., Ma, C., Meredith, N. P., Horne, R. B., Thorne, R. M., Heynderickx, D., & Anderson, R. R. (2002). Model of the energization of outer-zone electrons by whistler-mode chorus during the October 9, 1990 geomagnetic storm. *Geophysical Research Letters*, 29(24), 2174. <https://doi.org/10.1029/2002GL016039>
- Summers, D., Ni, B., & Meredith, N. P. (2007). Timescales for radiation belt electron acceleration and loss due to resonant wave-particle interactions: 2. Evaluation for VLF chorus, ELF hiss, and electromagnetic ion cyclotron waves. *Journal of Geophysical Research*, 112, A04207. <https://doi.org/10.1029/2006JA011993>
- Summers, D., Shi, R., Engebretson, M. J., Oksavik, K., Manweiler, J. W., & Mitchell, D. G. (2017). Energetic proton spectra measured by the Van Allen Probes. *Journal of Geophysical Research: Space Physics*, 122, 10,129–10,144. <https://doi.org/10.1002/2017JA024484>
- Summers, D., & Thorne, R. M. (2003). Relativistic electron pitch-angle scattering by electromagnetic ion cyclotron waves during geomagnetic storms. *Journal of Geophysics Research*, 108(A4), 1143. <https://doi.org/10.1029/2002JA009489>
- Theodoridis, G. C., & Paolini, F. R. (1967). Pitch angle diffusion of relativistic outer belt electrons. *Annales Geophysicae*, 23, 375.
- Thorne, R. M. (2010). Radiation belt dynamics: The importance of wave-particle interactions. *Geophysical Research Letters*, 37, L22107. <https://doi.org/10.1029/2010GL044990>
- Thorne, R. M., Li, W., Ni, B., Ma, Q., Bortnik, J., Chen, L., et al. (2013). Rapid local acceleration of relativistic radiation belt electrons by magnetospheric chorus. *Nature*, 504(7480), 411–414. <https://doi.org/10.1038/nature12889>
- Turner, D. L., Shprits, Y., Hartinger, M., & Angelopoulos, V. (2012). Explaining sudden losses of outer radiation belt electrons during geomagnetic storms. *Nature Physics*, 8(3), 208–212. <https://doi.org/10.1038/nphys2185>
- Usanova, M. E., Drozdov, A., Orlova, K., Mann, I. R., Shprits, Y., Robertson, M. T., et al. (2014). Effect of EMIC waves on relativistic and ultrarelativistic electron populations: Ground-based and Van Allen Probes observations. *Geophysical Research Letters*, 41, 1375–1381. <https://doi.org/10.1002/2013GL059024>
- Usanova, M. E., Mann, I. R., Rae, I. J., Kale, Z. C., Angelopoulos, V., Bonnell, J. W., et al. (2008). Multipoint observations of magnetospheric compression-related EMIC Pc1 waves by THEMIS and CARISMA. *Geophysical Research Letters*, 35, L17S25. <https://doi.org/10.1029/2008GL034458>
- Xiao, F., Chen, L., He, Y., Su, Z., & Zheng, H. (2011). Modeling for precipitation loss of ring current protons by electromagnetic ion cyclotron waves. *Journal of Atmospheric and Solar-Terrestrial Physics*, 73(1), 106–111. <https://doi.org/10.1016/j.jastp.2010.01.007>
- Yahnin, A. G., Yahnina, T. A., Raita, T., & Manninen, J. (2017). Ground pulsation magnetometer observations conjugated with relativistic electron precipitation. *Journal of Geophysical Research: Space Physics*, 122, 9169–9182. <https://doi.org/10.1002/2017JA024249>
- Yahnin, A. G., Yahnina, T. A., Semenova, N. V., Gvozdevsky, B. B., & Pashin, A. B. (2016). Relativistic electron precipitation as seen by NOAA POES. *Journal of Geophysical Research: Space Physics*, 121, 8286–8299. <https://doi.org/10.1002/2016JA022765>
- Yando, K., Millan, R. M., Green, J. C., & Evans, D. S. (2011). A Monte Carlo simulation of the NOAA POES medium energy proton and Electron detector instrument. *Journal of Geophysics Research*, 116, A10231. <https://doi.org/10.1029/2011JA016671>
- Yuan, Z., Deng, X., Lin, X., Pang, Y., Zhou, M., Décréau, P. M. E., et al. (2010). Link between EMIC waves in a plasmaspheric plume and a detached sub-auroral proton arc with observations of cluster and IMAGE satellites. *Geophysical Research Letters*, 37, L07108. <https://doi.org/10.1029/2010GL042711>
- Zhang, X.-J., Li, W., Ma, Q., Thorne, R. M., Angelopoulos, V., Bortnik, J., et al. (2016). Direct evidence for EMIC wave scattering of relativistic electrons in space. *Journal of Geophysical Research: Space Physics*, 121, 6620–6631. <https://doi.org/10.1002/2016JA022521>